Original Article



Arctigenin Prevents Metabolic Dysfunction-associated Steatohepatitis by Inhibiting NLRP3/GSDMD-N Axis in Macrophages



Rui Xue¹, Lu Jiang², Qian-Ren Zhang¹, Qing-Jing Wang¹, Rui-Xu Yang¹, Tian-Yi Ren¹, Qin Pan^{1,2*} and Jian-Gao Fan^{1,2*}

¹Department of Gastroenterology, Xinhua Hospital Affiliated to Shanghai Jiao Tong University School of Medicine, Shanghai, China; ²Shanghai Institute of Pediatric Research, Shanghai Key Laboratory of Pediatric Gastroenterology and Nutrition, Xinhua Hospital, Shanghai Jiao Tong University, School of Medicine, Shanghai, China

Received: April 01, 2025 | Revised: June 11, 2025 | Accepted: July 17, 2025 | Published online: August 25, 2025

Abstract

Background and Aims: Metabolic dysfunction-associated steatohepatitis (MASH) represents a critical step in the progression from simple fatty liver disease to more severe conditions such as cirrhosis and hepatocellular carcinoma, and it remains difficult to treat. Arctigenin (ATG), a monomer of Fructus Arctii, exhibits anti-inflammatory activity. Therefore, we aimed to examine its potential protective role against MASH and explore the underlying mechanisms. **Methods:** Male C57BL/6 mice were divided into four groups: control, MASH, low-dose ATG (30 mg/kg/day), and high-dose ATG (120 mg/kg/day). MASH was induced through a cholinedeficient, L-amino acid-defined high-fat diet for eight weeks, with concurrent preventive ATG administration. Liver injury, lipid metabolism, inflammation, oxidative stress, and fibrosis were assessed. Network pharmacology was employed to identify the potential protective mechanisms of ATG. Key factors were evaluated in vitro to verify the ATG targets. Results: ATG administration prevented the progression of MASH in a dose-dependent manner. High-dose ATG significantly reduced hepatic macrophage and neutrophil infiltration, serum enzyme levels, and lipid peroxidation, while enhancing antioxidant enzyme activity. Mechanistic network pharmacology identified modulation of the NLR family pyrin domain containing 3 (NLRP3) inflammasome as the central pathway underlying ATG's bioactivity. Functional analyses in lipopolysaccharide-stimulated RAW264.7 cells confirmed that ATG inhibited NLRP3 expression, pyroptosis-related protein cleavage (hereinafter referred to as GSDMD-N), and pro-inflammatory chemokine production in a concentrationdependent manner. Notably, ATG disrupted NLRP3/GSDMD-

Keywords: Metabolic dysfunction-associated steatohepatitis; Arctigenin; Inflammation; Macrophage; NLR family pyrin domain containing 3; c-FOS. *Correspondence to: Jian-Gao Fan and Qin Pan, Department of Gastroenterolo-

N axis activity in macrophages without causing cellular toxicity. *Conclusions:* ATG may inhibit the inflammatory cascade primarily by targeting macrophage NLRP3 inflammasomes, thereby preventing the progression of MASH.

Citation of this article: Xue R, Jiang L, Zhang QR, Wang QJ, Yang RX, Ren TY, *et al.* Arctigenin Prevents Metabolic Dysfunction-associated Steatohepatitis by Inhibiting NLRP3/GSDMD-N Axis in Macrophages. J Clin Transl Hepatol 2025; 13(10):809–824. doi: 10.14218/JCTH.2025.00141.

Introduction

Metabolic dysfunction-associated fatty liver disease (MAFLD), previously referred to as nonalcoholic fatty liver disease (NAFLD), accounts for the largest proportion of chronic liver disease worldwide and affects diverse populations across all age groups. MAFLD comprises a spectrum of liver disorders, including metabolic dysfunction-associated fatty liver (MAFL) and metabolic dysfunction-associated steatohepatitis (MASH). MASH can progress to liver fibrosis or even hepatocellular carcinoma. Although recent reports suggest that resmetirom, a thyroid receptor β agonist, may improve MASH, options for clinical intervention remain limited, and further research is necessary.

Recent studies have highlighted the pivotal role of hepatic macrophages in the progression of MAFLD,³ as their interactions with other hepatic cells can amplify inflammation and promote fibrosis. Macrophages, which are derived from resident Kupffer cells and circulating monocytes, can acquire either anti-inflammatory (M2) or pro-inflammatory (M1) phenotypes upon exposure to environmental stimuli.⁴ M1 macrophages exacerbate liver inflammation by producing inflammation-inducing cytokines that facilitate immune responses.^{5–8} Conversely, reducing macrophage infiltration or inducing macrophage polarization toward the M2 phenotype can improve MAFLD.^{6,9–12} These findings underscore macrophages as key therapeutic targets for MASH.

Traditional Chinese medicine and various monomeric compounds extracted from Chinese herbal medicines have garnered attention in recent decades for the prevention

^{*}Correspondence to: Dian-Gao Fan and Qin Pan, Department of Gastroenterology, Xinhua Hospital Affiliated to Shanghai Jiao Tong University School of Medicine; Shanghai Institute of Pediatric Research, Shanghai Key Laboratory of Pediatric Gastroenterology and Nutrition, Xinhua Hospital, Shanghai Jiao Tong University, School of Medicine, 1665 Kong Jiang Road, Shanghai 200092, China. ORCID: https://orcid.org/0000-0002-8618-6402 (JGF) and https://orcid.org/0000-0001-5855-4952 (QP). Tel: +86-21-25077340 (JGF) and +86-18918020021 (QP), Fax: +86-21-65795173 (JGF) and +86-21-65794273 (QP), E-mail: fanjiangao@xinhuamed.com.cn (JGF) and panqin@xinhuamed.com.cn (QP).

and treatment of MAFLD.¹³ Arctigenin (ATG), a glycoside compound derived from *Arctium lappa*, has demonstrated pharmacological effects, including improving glucose tolerance and lipid metabolism, as well as mitigating inflammation.^{14–17} However, its effects on MASH remain largely unexplored. Previous studies suggest that ATG can suppress inflammation and lipid peroxidation in hepatocytes, providing evidence of its ability to alleviate liver injury.¹⁷ Furthermore, ATG reportedly inhibits the assembly of the NLR family pyrin domain containing 3 (NLRP3) inflammasome in colonic macrophages, possibly by downregulating carnitine palmitoyltransferase-1 expression.¹⁸ Thus, ATG may regulate inflammatory and oxidative stress pathways, particularly in macrophages, which play a central role in the progression of MAFL to MASH.

Therefore, we established a rodent model using a choline-deficient, L-amino acid-defined high-fat diet (CDAHFD) and conducted an *in vivo* study to explore whether ATG plays a preventive role in MASH. Mechanistic analyses of ATG treatment were performed, focusing on the regulation of the NLRP3 inflammasome, which mediates hepatic inflammation and fibrosis.

Methods

Animal study

Four groups (n = 10 per group) were randomly assigned from 40 male C57BL/6 mice, aged eight weeks and weighing 20-25 g. The animals were housed in an environment with a specific circadian rhythm (12 h of light and 12 h of darkness) and a controlled temperature ($21-23^{\circ}$ C). They had access to food and water ad libitum. All animal experiments were approved by the Institutional Animal Care and Use Committee of Xinhua Hospital affiliated to Shanghai Jiao Tong University School of Medicine.

Following a week of adaptive feeding, the 40 mice were randomized into the following groups: control, model, low-dose ATG treatment (30 mg/kg per day), and high-dose ATG treatment (120 mg/kg per day) (Cat: HY-N0035, Med Chem Express®, Shanghai, China). The control group was exposed to a standard chow diet and vehicle treatment (10% dimethyl sulfoxide (DMSO)) (Cat: 67-68-5, Sigma-Aldrich®, Missouri, USA) for eight weeks. The model group was fed a CDAHFD (Cat: TP36225MCD, Trophic Co., Nantong, China) during the same period, with vehicle therapy (10% DMSO). The two treatment groups were also fed CDAHFD ad libitum, with intragastric administration of 30 or 120 mg/kg ATG. Both vehicle and ATG treatments were administered once daily *via* intragastric injection for eight weeks.

After 12 h of fasting and under isoflurane anesthesia, all animals were sacrificed at the end of the 8^{th} week. Blood samples were collected from the retroorbital sinus. Cervical dislocation was performed, and the livers were immediately dissected on ice and weighed. Before analysis, liver samples were snap-frozen in liquid nitrogen and stored at -80° C. Additional liver samples were fixed in 4% formalin for subsequent experiments.

Biochemical analyses

Serum was extracted from blood samples by centrifugation for 15 m at 4°C and 4,000 rpm. The activities of alanine aminotransferase (Cat: 20152400366, ShenSuoYoufu Medical Diagnostic Products, Shanghai, China) and aspartate transaminase (Cat: 20152400367, ShenSuoYoufu Medical Diagnostic Products, Shanghai, China)¹⁹ were measured using kits according to the manufacturer's instructions. The

serum levels of free fatty acid (FFA) (Cat: 633-52001, FUJI-FILM Wako Pure Chemical Corporation, Japan)²⁰ and very low density lipoprotein (VLDL) (Cat: ml037709, mlbio, Shanghai, China)²¹ were measured using the respective kits. Hepatic levels of triglyceride (TG) (Cat: E1015) and total cholesterol (Cat: E1015) were quantified using assay kits (Applygen Technologies Inc., Beijing, China).²² Malondialdehyde (MDA) (Cat: A003-1-2), catalase (CAT) (Cat: A007-1-1), and superoxide dismutase (SOD) (Cat: A001-1-1) levels in the liver were analyzed using commercial kits (Nanjing Jiancheng Bioengineering Institute, Nanjing, China).²³ Briefly, liver samples were homogenized on ice, and supernatants were collected after centrifugation for subsequent analysis. The total protein concentration in the samples was used as a reference for final concentrations.

Histological determination

Following paraformaldehyde fixation, each liver tissue sample was embedded in paraffin and sliced. Hematoxylin & eosin staining, Masson's trichrome staining, and Sirius red staining were performed using commercial kits (Servicebio®, Wuhan, China). Sections frozen in optimum cutting temperature compound were snap-frozen in liquid nitrogen and subjected to Oil Red O staining using a commercial kit (Servicebio®, Wuhan, China) according to the manufacturer's guidelines. The NAFLD activity score (NAS), which evaluates lobular inflammation, hepatocyte ballooning, and steatosis, was used for histological analysis. S

Immunohistochemical assays

Paraffin sections were deparaffinized and rehydrated, and antigen retrieval was performed using citrate buffer (0.01 M, pH 6.0).²⁶ The sections were incubated overnight with antibodies specific to F4/80 (GB11027, Servicebio®, 1:500), myeloperoxidase (GB150006, Servicebio®, 1:500), and alpha-smooth muscle actin (α-SMA) (GB111364, Servicebio®, 1:300), respectively. After incubation with the secondary antibody conjugated with HRP for 60 m at room temperature, the sections were washed three times for 5 m each using phosphate-buffered saline (PBS). The DAB chromogen reaction was stopped by washing with running water. Hematoxylin counterstaining was applied for 30 s, followed by rinsing with water, dehydration, and mounting with resin. The slides were viewed under a digital microscope camera (Eclipse E100, Nikon®, Japan). The acquired images were analyzed using ImageJ 1.46r software (National Institutes of Health, Bethesda, MD, USA).

Real-time quantitative polymerase chain reaction

Total RNA was extracted from liver tissues or cells using an RNA purification kit (Cat: B0004D, Ezbioscience®, Roseville, USA) and quantified using the QuantStudio Dx system (Applied Biosystems®, Waltham, Massachusetts, USA). DNA templates were obtained by reverse transcription of RNA using a color reverse transcription kit (Cat: A0010CGQ, Ezbioscience®, Roseville, USA). Relative mRNA expression was quantified using the SYBR GREEN Master Mix reagent kit (Cat: A0012-R2, Ezbioscience®, Roseville, USA). Gene expression levels were normalized against 18S rRNA expression. The 2- $\Delta\Delta$ Ct method was used for data analysis. Primer sequences are listed in Table 1.

Immunofluorescence assays

Liver tissue sections were prepared by deparaffinization, rehydration, and antigen retrieval with EDTA buffer (0.01 M, pH 9.0), followed by PBS washes. Endogenous peroxidase

Table 1. Primers for real-time quantitative polymerase chain reaction (mus)

Gene name	Forward primer	Reverse primer		
a-SMA	5'-TGCTTCCTCCTCCTTTG-3'	5'-GAAGTACTGCCGTTTTCCCC-3'		
TGF-β	5'-CTGAACCAAGGAGACGGAATA-3'	5'-GGAAGGGCCGGTTCATGT-3'		
VIMENTIN	5'-CGGAAAGTGGAATCCTTGCAGG-3'	5'-AGCAGTGAGGTCAGGCTTGGAA-3'		
COL1A1	5'-CCAGCAAACAAAGGCAATGC-3'	5'-GGTGCTGGGTAGGGAAGTAG-3'		
COL2A1	5'-CAACTCAGCTCGCCTTCATG-3'	5'-CTCATCCAGGTACGCAATGC-3'		
COL3A1	5'-TGACTGTCCCACGTAAGCAC-3'	5'-GAGGGCCATAGCTGAACTGA-3'		
NLRP3	5'-TCACAACTCGCCCAAGGAGGAA-3'	5'-AAGAGACCACGGCAGAAGCTAG-3'		
IL-1β	5'-TCCAGGATGAGGACATGAGCAC-3'	5'-GAACGTCACACACCAGCAGGTTA-3'		
iNOS	5'-GAGACAGGGAAGTCTGAAGCAC-3'	5'-CCAGCAGTAGTTGCTCCTCTTC-3'		
TNF-a	5'-CAGGAGGGAGAACAGAAACTCCA-3'	5'-CCTGGTTGGCTGCTT-3'		
CYBA	5'-GCTCATCTGTCTGCTGGAGTATC-3'	5'-GGACGTAGTAATTCCTGGTGAG-3'		
NOX2	5'-TGGCGATCTCAGCAAAAGGTGG-3'	5'-GTACTGTCCCACCTCCATCTTG-3'		
NRF2	5'-AGAACGAGAGGACACCTGGTCA-3'	5'-GCTTCTGGGATGCTGGAAACG-3'		
CCL2	5'-TTAAAAACCTGGATCGGAACCAA-3'	5'-TTAAAAACCTGGATCGGAACCAA-3'		
CXCL1	5'-TCCAGAGCTTGAAGGTGTTGCC-3'	5' -AACCAAGGGAGCTTCAGGGTCA-3'		
CXCL3	5' -TGAGACCATCCAGAGCTTGACG-3'	5' -CCTTGGGGGTTGAGGCAAACTT-3'		
CXCL5	5' -CCGCTGGCATTTCTGTTGCTGT-3'	5' -CAGGGATCACCTCCAAATTAGCG-3'		
CXCL15	5' -GGTGATATTCGAGACCATTTACTG-3'	5' -GCCAACAGTAGCCTTCACCCAT-3'		
SREBF1	5' -CGACTACATCCGCTTCTTGCAG-3'	5' -CCTCCATAGACACATCTGTGCC-3'		
FASN	5' -CACAGTGCTCAAAGGACATGCC-3'	5' -CACCAGGTGTAGTGCCTTCCTC-3'		
PPARa	5' -ACCACTACGGAGTTCACGCATG-3'	5' -GAATCTTGCAGCTCCGATCACAC-3'		
CPT1a	5' -GGCATAAACGCAGAGCATTCCTG-3'	5' -CAGTGTCCATCCTCTGAGTAGC-3'		
CD206	5' -GTTCACCTGGAGTGATGGTTCTC-3'	5' -AGGACATGCCAGGGTCACCTTT-3'		
ARG1	5' -CATTGGCTTGCGAGACGTAGAC-3'	5' -GCTGAAGGTCTCTTCCATCACC-3'		
CD36	5' -GGACATTGAGATTCTTTTCCTCTG-3'	5' -GCAAAGGCATTGGCTGGAAGAAC-3'		
ACSL1	5' -ATCAGGCTGCTTATGGACGACC-3'	5' -CCAACAGCCATCGCTTCAAGGA-3'		
FATP1	5' -TGCCACAGATCGGCGAGTTCTA-3'	5' -AGTGGCTCCATCGTGTCCTCAT-3'		
ACOX1	5' -GCCATTCGATACAGTGCTGTGAG-3'	5' -CCGAGAAAGTGGAAGGCATAGG-3'		
SLC27A5	5' -CTGCGGTACTTGTGTAACGTCC-3'	5' -TCCGAATGGGACCAAAGCGTTG-3'		
ACC1	5' -GTTCTGTTGGACAACGCCTTCAC-3'	5' -GGAGTCACAGAAGCAGCCCATT-3'		
APOB	5' -GCATGAGTATGCCAATGGTCTCC-3'	5' -CTGGTTGCCATCTGAAGCCATG-3'		
APOE	5' -GAACCGCTTCTGGGATTACCTG-3'	5' -GCCTTTACTTCCGTCATAGTGTC-3'		
MTTP	5' -CCAGGAAAGGTTCCTCTATGCC-3'	5' -GACTCTCTGATGTCGTTGCTTGC-3'		
TM6SF2	5' -GGTATTTGCTGGAGCCATTGGC-3'	5' -CCAGTGCCAATAGCAGGTTGCT-3'		
PNPLA3	5' -AGACAAGGTGCCAGTCAGCCTA-3'	5' -GAGGTTGCAGACTTTGCTCAGG-3'		
SPTLC2	5' -CCAGACTGTCAGGAGCAACCAT-3'	5' -CTTCTTGTCCGAGGCTGACCAT-3'		
ACER2	5' -GAGGACAACTACACTATCGTGCC-3'	5' -TAGATGCCGCTGTTGAAGCACG-3'		
ASAH1	5' -GGATGTTCGGAAGGAAAGATGCC-3'	5' -AACCCTCTCCAGACTTCTTGCC-3'		
CERS2	5' -CCTTCTACTGGTCCCTGCTCTT-3'	5' -TGGCAAACCAGGAGAAGCAGAG-3'		
CYP7A1	5' -CACCATTCCTGCAACCTTCTGG-3'	5' -ATGGCATTCCCTCCAGAGCTGA-3'		

(continued)

Table 1. (continued)

Gene name	Forward primer	Reverse primer		
HMGCR	5' -GCTCGTCTACAGAAACTCCACG-3'	5' -GCTTCAGCAGTGCTTTCTCCGT-3'		
SGMS1	5' -GCATAGTTGGCACGCTGTACCT-3'	5' -TAAGCCACCTCCAGCAATGAGC-3'		
18S	5'-ACGGAAGGGCACCACCAGGA-3'	5'-CACCACCACCGGAATCG-3'		

α-SMA, alpha-smooth muscle actin; TGF-β, transforming growth factor-beta; COL1A1, collagen type I alpha 1 chain; COL2A1, collagen type II alpha 1 chain; IL-1β, interleukin-1β; iNOS, inducible nitric oxide synthase; TNF-α, tumor necrosis factor-α; CYBA, cytochrome B-245 alpha chain; NOX2, NADPH oxidase 2; NRF2, nuclear factor erythroid 2-related factor 2; CCL2, C-C motif chemokine 2; CXCL1, C-X-C motif chemokine ligand 1; CXCL3, C-X-C motif chemokine ligand 3; CXCL5, C-X-C motif chemokine ligand 5; CXCL15, C-X-C motif chemokine ligand 15; SREBF1, sterol regulatory element binding transcription factor 1; FASN, fatty acid synthase; PPARα, peroxisome proliferator activated receptor alpha; CPT1α, carnitine palmitoyltransferase 1 alpha; ARG1, arginase 1; CD36, cluster of differentiation 36; ACSL, acyl-CoA synthetase long chain family member 1; FATP1, fatty acid transport protein 1; ACOX1, acyl-CoA oxidase 1; SLC27A5, solute carrier family 27 member 5; ACC1, acetyl-CoA carboxylase 1; APOB, apolipoprotein B; APOE, apolipoprotein E; MTTP, microsomal triglyceride transfer protein; TM6SF2, transmembrane 6 superfamily member 2; PNPLA3, patatin like domain 3, 1-acylglycerol-3-phosphate o-acyltransferase; SPTLC2, serine palmitoyltransferase long chain base subunit 2; ACER2, alkaline ceramidase 2; ASAH1, N-acylsphingosine amidohydrolase 1; CERS2, ceramide synthase 2; CYP7A1, cytochrome P450 family 7 subfamily A member 1; HMGCR, 3-hydroxy-3-methylglutaryl-CoA reductase; SGMS1, sphingomyelin synthase 1.

activity was suppressed with 3% hydrogen peroxide, and the sections were blocked with 3% BSA. Primary antibodies against CD86 (19589, Cell Signaling Technology, CST®; 1:400 in 3% BSA) and α-SMA (ab124964, Abcam®; 1:2,000 in 3% BSA) were incubated overnight. After PBS washes, secondary antibody (ab205718, Abcam®; 1:4,000 in PBS) was applied at 37°C for 45 m, followed by CY5 tyramide staining (11066, AAT Bio®; 1:400 in 0.003% H2O2) for 10 m. The slides were washed, stripped in 42°C stripping buffer for 20 m, and re-blocked. The sections were then incubated overnight with primary antibodies against NLRP3 (PA5-79740, ThermoFisher®; 1:100 in 3% BSA). After PBS washes, the secondary antibody (Alexa Fluor™ 488-conjugated donkey anti-rabbit IgG, A21206, ThermoFisher®; 1:400 in PBS) was applied at 37°C for 45 m. Each sample was stained with DAPI, followed by washing with water to terminate the reaction. Fluorescence images were acquired using a BX53 microscope (Olympus®, Japan) and analyzed using ImageJ 1.46r (National Institutes of Health, Bethesda, MD, USA).²⁸

Target analysis of ATG

PubChem (https://pubchem.ncbi.nlm.nih.gov/) provides the chemical structure and canonical SMILES of ATG. These data were subsequently entered into multiple target prediction tools, including the PharmMapper server (https://www.lilabecust.cn/pharmmapper/),²⁹ Similarity Ensemble Approach (https://sea.bkslab.org/),³⁰ and SwissTargetPrediction (http://www.swisstargetprediction.ch/),31 to identify potential molecular targets associated with ATG. Additional targets were obtained from relevant scientific literature. Overlapping targets between ATG and MAFLD were identified using the Venny online tool (https://cloud.oebiotech.com/#/bio/tools). Protein-protein interaction networks for the intersecting targets were analyzed using the STRING database (https:// string-db.org/) and subjected to visualization and topological analyses using Cytoscape 3.7.2.32 Further investigation of the molecular mechanisms underlying ATG's therapeutic effects on MAFLD was conducted through pathway enrichment based on the Kyoto Encyclopedia of Genes and Genomes database, Reactome pathway enrichment analysis, and Gene Ontology analysis. These analyses were performed using the Oebiotech bioinformatics platform (https://cloud.oebiotech. com/#/bio/tools), focusing on molecular functions, cellular components, biological processes, and pathways relevant to MAFLD-associated targets. The Liver Cell Atlas (https://livercellatlas.org/) was used to analyze NLRP3 expression in different liver cells based on data provided by the Liver Cell Atlas (Mouse NAFLD Atlas).33 Molecular docking was carried out via CB-Dock2 (https://cadd.labshare.cn/cb-dock2/index.

php).³⁴ Transcription factors of the NLRP3 gene were predicted using the UCSC-JASPAR (https://genome.ucsc.edu/index. html),³⁵ Chip-Altas (https://chip-atlas.org/),³⁶ Cistrome DB (http://cistrome.org/db/),³⁷ hTFtarget (https://guolab.wch-scu.cn/hTFtarget/#!/),³⁸ and NetworkAnalyst (https://www.networkanalyst.ca/)³⁹ databases.

Western blotting

Phosphatase inhibitors (Cat: 20109ES05, Yeasen®, Shanghai, China) along with a protease inhibitor cocktail (Cat: ST505, Beyotime®, Shanghai, China) were added to RIPA buffer before the liver tissues were lysed. The BCA assay (Cat: P0012, Beyotime®, Shanghai, China) was employed to determine the total protein content. Proteins separated by SDS-PAGE were transferred onto polyvinylidene difluoride (PVDF) membranes using a small vertical gel electrophoresis machine (Tanon®, Shanghai, China).40 After blocking with 5% fat-free milk, the membranes were incubated with primary antibodies overnight at 4°C. Horseradish peroxidase-labeled secondary antibodies were used for detection. Chemiluminescent signals were collected and assessed using the ChemiDOC XRS+ imaging system (Bio-Rad Laboratories®, California, USA) and Image Lab 6.1.0 software. The following antibodies were used for Western blot analysis: NLRP3 (ab263899, Abcam®), GAPDH (2118, CST®), interleukin (IL)-1β (12242, CST®), Gasdermin D (GSDMD) (39754, CST®), c-Fos (66590-1-Ig, Proteintech®), a-Tubulin (66031-1-Ig, Proteintech®), and Lamin B1 (AF1408, Beyotime®). GAPDH, a-Tubulin, and Lamin B1 served as controls.

Cell culture, cell viability assay, and treatment

Mouse monocytic macrophage RAW264.7 cells (Cell Bank of the Chinese Academy of Sciences, Shanghai, China) were cultured in DMEM with 10% fetal bovine serum (Cat: 16000-044, Gibco®, Waltham, Massachusetts, USA) and penicillin/streptomycin (Cat: 60162ES76, YEASEN®, Shanghai, China).

Cell viability was evaluated using the Cell Counting Kit-8 assay (Cat: C0037, Beyotime®, Shanghai, China). Briefly, RAW264.7 cells were seeded at 1.5×10^4 cells/well in 96-well plates, and dose ranges from 0–100 μM ATG were added to the plates for 24 h. Following treatment, each well received 10 μL of the Cell Counting Kit-8 reagent and was incubated at 37°C for an additional hour. Absorbance was measured at 450 nm. 41 Cells were exposed to 100 ng/mL lipopolysaccharide (LPS) (Cat: 297-473-0, Sigma-Aldrich®, Missouri, USA) for 24 h, either with or without varying doses of ATG, to induce inflammation.

Cellular thermal shift assay (CETSA)

RAW264.7 pellets were collected and washed twice with icecold PBS, followed by resuspension in protein lysis buffer (containing 1× protease inhibitor cocktail) and incubation on ice for 15 m. Cell lysis was achieved through sonication, and the lysates were clarified by centrifugation (20,000 \times g, 10 m, 4°C) to collect the supernatant. After quantifying the protein concentration using the BCA assay, samples were diluted with distilled water to achieve uniform protein concentrations. The normalized lysates were equally divided into two aliquots: one treated with ATG (100 µM final concentration) and the other with an equal volume of DMSO. After 1 h of incubation at room temperature, each aliquot was subdivided into five equal portions and subjected to 10 m incubations at distinct temperatures (49°C, 52°C, 55°C, 58°C, or 61°C), then immediately chilled on ice. Post-heating clarification was performed by centrifugation (20,000 \times g, 10 m, 4°C), and the soluble protein supernatants were mixed with equal volumes of 2× loading buffer, denatured at 99°C for 10 m, and stored at -80°C prior to Western blot analysis of NLRP3 expression.42

Nuclear and cytoplasmic protein extraction

RAW264.7 cells were seeded into 6-well plates at 2×10⁵ cells/well and allowed to attach for 24 h. The cells were then divided into three groups: Control group, LPS-treated group (100 ng/mL LPS), and ATG-treated group (100 µM) for 4 h, followed by washing twice with ice-cold PBS. The Nuclear and Cytosolic Protein Extraction Kit (Cat: P0027, Beyotime®, Shanghai, China) was used to isolate cytosolic and nuclear proteins. 43 First, the cells were collected into 1.5 mL microcentrifuge tubes. Cytosolic protein extraction reagent A, containing protease inhibitor cocktail and phosphatase inhibitor cocktail, was added to each tube. Vortex mixing was performed for 5 s at the highest speed, followed by incubation on ice for 10–15 m. Cytoplasmic protein extraction reagent B was added, followed by vortex mixing at maximum speed for 5 s, then an ice bath for 1 m. After vortex mixing for 5 s, centrifugation was performed at 12,000-16,000 g at 4°C for 5 m. The supernatant containing the cytoplasmic proteins was aspirated into a pre-cooled tube. For the pellet, residual supernatant was aspirated, and 50 µL of nuclear protein extraction reagent, containing protease inhibitor cocktail and phosphatase inhibitor cocktail, was added. The mixture was vortexed for 15-30 s and placed in an ice bath. Every 1-2 m, vortex mixing was repeated vigorously at high speed for 30 m. Finally, centrifugation was performed at 12,000-16,000 g for 10 m at 4°C, and the supernatant containing the nuclear protein was aspirated into a pre-cooled tube. Cytosolic and nuclear fractions were stored at -80°C until required.

Statistical analysis

Data are presented as mean \pm standard error. The statistical significance of the parametric variables was investigated using the unpaired Student's t-test between two groups, and one-way ANOVA for comparisons among multiple groups. Multiple comparisons among multiple groups were performed using Tukey's post hoc test. Statistical analyses were conducted using GraphPad Prism (version 9.0). Statistical significance was indicated by a p-value < 0.05.

Results

ATG prevented rodent MASH induced by CDAHFD

Compared with the control group, the body mass of the other

groups that were fed the CDAHFD was reduced during the initial two weeks and remained at a significantly lower level until the end of the 8th week (Fig. 1A and B). However, their liver index and TG content were significantly higher than those of the control group (Fig. 1C and D). No significant difference in liver total cholesterol content was observed among the four groups (Fig. 1E). In mice with or without ATG administration, similar alterations in body weight, liver index, and chemical indices were observed after the CDAHFD (Fig. 1A–E, Supplementary Fig. 1A and B). No significant differences were observed in the expression of key genes related to lipid metabolism, including the metabolism of FFA, cholesterol, VLDL, and ceramide (Supplementary Fig. 1C–F).

The significant increase in serum alanine aminotransferase and aspartate transaminase levels indicated that the eightweek CDAHFD treatment caused liver injury (Fig. 1F and G). After ATG prophylaxis, there was a significant improvement in liver enzymes in both the low- and high-dose groups (Fig. 1F and G). Histopathological staining revealed that the model group exhibited bullous steatosis, lobular inflammation, and limited hepatocyte ballooning (Fig. 1H). An NAS score > 5 in most mice (eight out of nine) met the diagnostic criteria for MASH (Fig. 1I). After ATG prophylaxis, both the low-dose (average NAS score = 4.978 ± 0.168) and high-dose groups (average NAS score = 4.125 ± 0.165) showed a decrease (Fig. 1I), mainly due to the attenuation of lobular inflammation. Moreover, the decrease in the NAS score was more significant in the high-dose group than in the low-dose group (Fig. 1I).

ATG reduced macrophage and neutrophil infiltration and ameliorated oxidative stress in MASH

Immunohistochemical staining was performed to determine the effects of ATG on the immune microenvironment in the liver. There were almost no neutrophils in the control group, while macrophages were mainly distributed along the hepatic sinusoids (Fig. 2A–C). In contrast, the hepatic lobules of the model group exhibited obvious infiltration of macrophages and neutrophils (Fig. 2A). Macrophages were enriched around hepatocytes with lipid droplets, forming a coronal structure (Fig. 2A). Neutrophils clumped together to form foci of inflammation (Fig. 2A). Compared to the model group, ATG prophylaxis led to much less infiltration of macrophages and neutrophils, with the most significant effect observed in the high-dose group (Fig. 2A–C).

Furthermore, the expression levels of inflammatory chemokines in the liver tissue were studied. The expressions of C-C motif chemokine 2 (Fig. 2D), C-X-C motif chemokine ligand (CXCL) 1 (Fig. 2E), CXCL15 (Fig. 2F), CXCL5 (Fig. 2G), and CXCL3 (Fig. 2H) were significantly upregulated after CDAHFD feeding, but this upregulation of pro-inflammatory genes did not occur in the low-dose and high-dose ATG prophylaxis groups (Fig. 2D–H).

Oxidative stress plays an important role in the progression of MASH. We assessed the level of oxidative stress in the liver by measuring the content or activity of oxidative products, MDA, and antioxidant enzymes (SOD and CAT). In contrast to the control group, the MDA concentration was significantly elevated in the liver homogenate of the model group (Fig. 2I). However, there was a dose-dependent decrease in MDA levels in both the low- and high-dose groups (Fig. 2I). The SOD and CAT tests showed that only the levels of antioxidant enzymes were significantly higher in the high-dose group than in the model group, whereas these indices displayed a tendency toward improvement in the low-dose group (Fig. 2J and K). By detecting the expression of oxidative stress-related genes, we found significantly upregulated levels of the

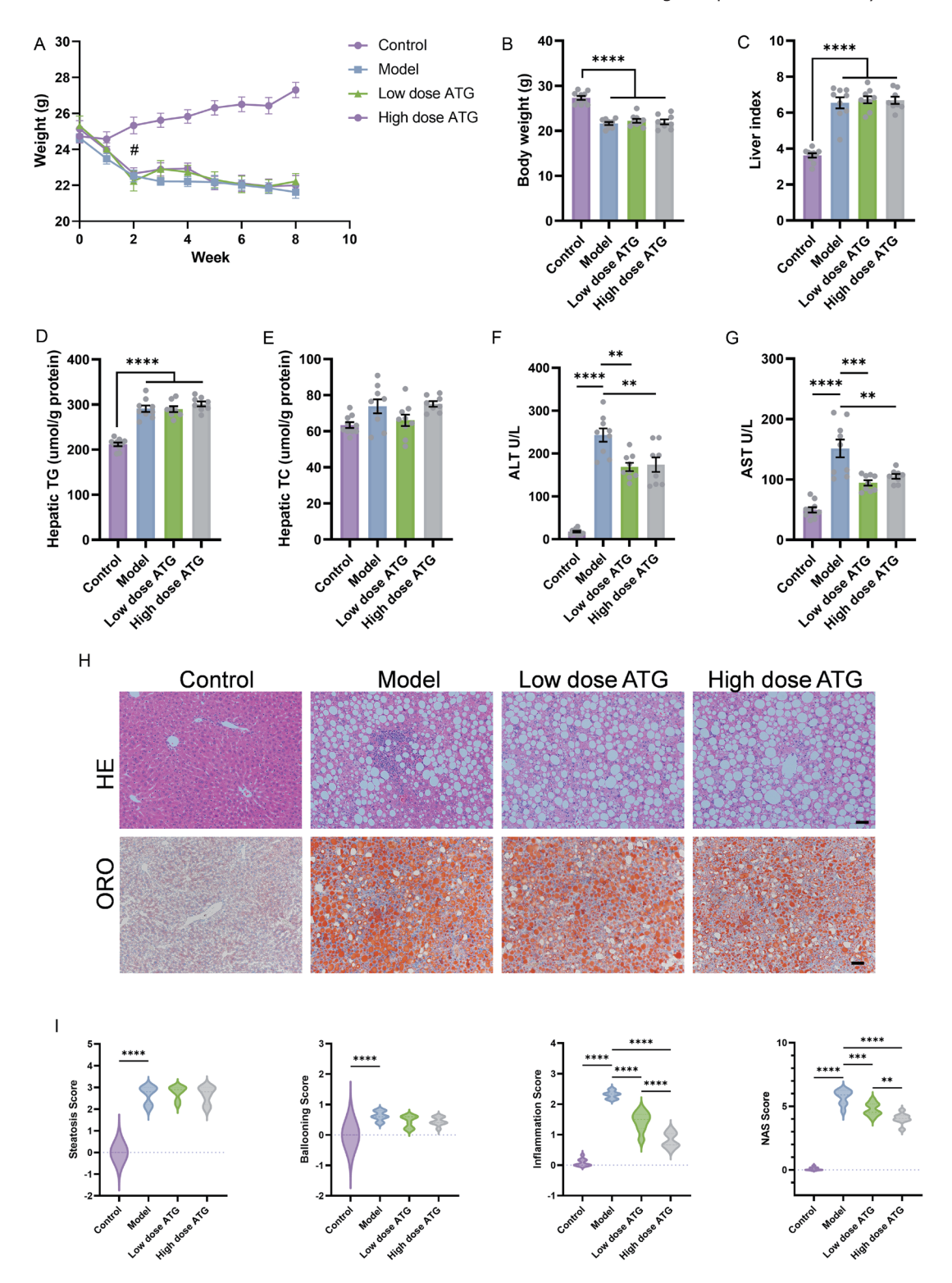


Fig. 1. Effects of ATG on MASH induced by choline-deficient, L-amino acid-defined, high-fat diet. (A) The dynamic changes in body weight were measured in the control, model, low-dose ATG-treatment, and high-dose ATG-treatment groups. #: Model, Low-dose ATG, and High-dose ATG compared to Control, p < 0.001. (B-C) Body weight (B) and liver index (C) at the end of eight weeks in the control, model, low-dose ATG-treatment, and high-dose ATG-treatment groups. (D-G) Liver contents of TG (D) and TC (E) and serum levels of ALT (F) and AST (G) of mice after eight weeks of intervention in four groups. (H-I) HE staining (scale bar: $100 \mu m$) (H, lower panel), and NAS score (I) of liver sections from each group after eight weeks of intervention. $n = 8-10 \mu m$) (H) bata are presented as mean \pm SEM. **p < 0.001, ****p < 0.001. ****p < 0.001. ATG, arctigenin; MASH, metabolic dysfunction-associated steatohepatitis; CDAHFD, choline-deficient, L-amino acid-defined, high-fat diet; TG, triglyceride; TC, total cholesterol; ALT, alanine aminotransferase; AST, aspartate aminotransferase; HE staining, hematoxylin & eosin staining; ORO staining, Oil Red O staining; NAS score, nonalcoholic fatty liver disease activity score; SEM, standard error of the mean.

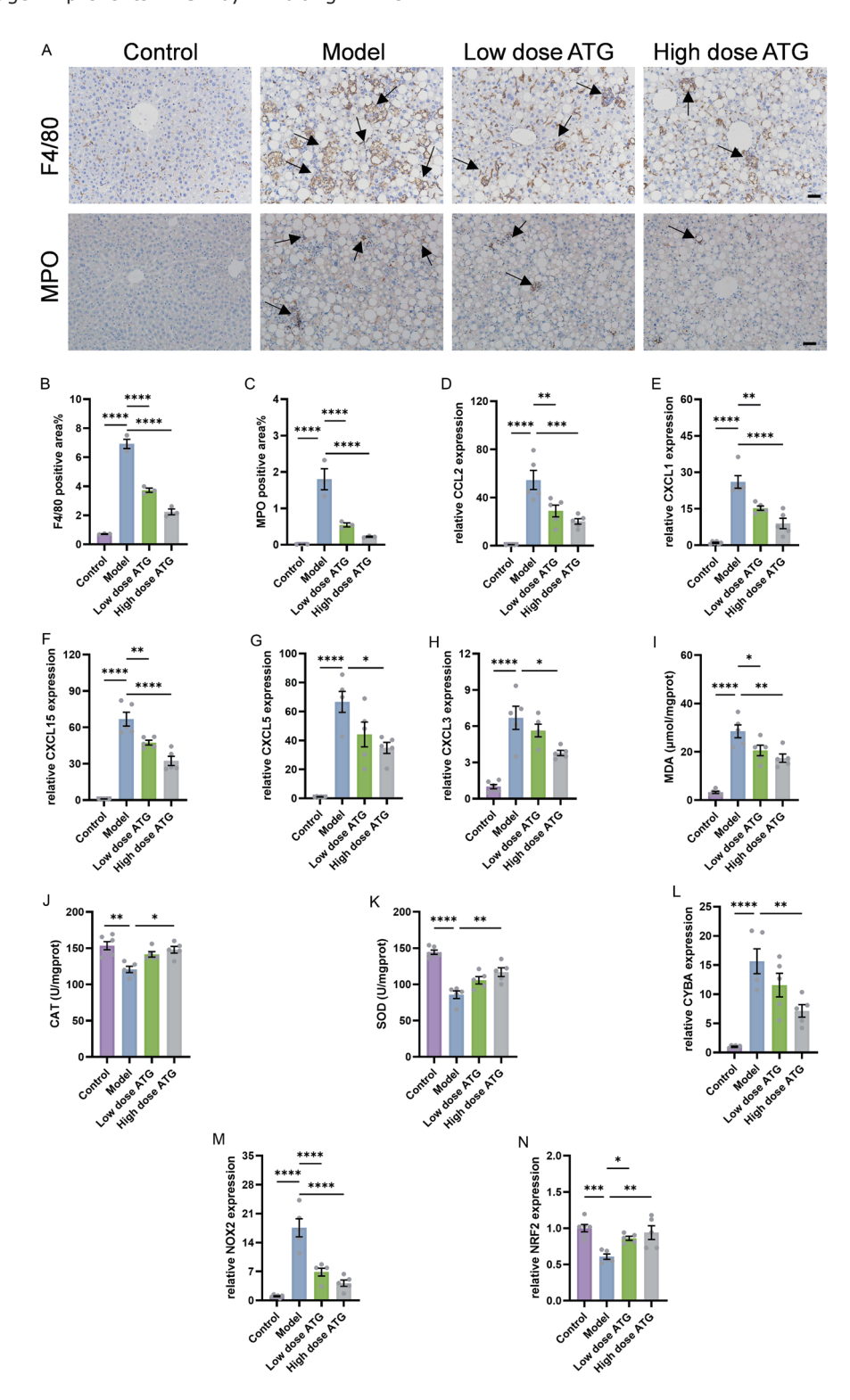


Fig. 2. Effects of ATG on neutrophil and macrophage accumulation and oxidative stress in MASH. (A–C) Immunohistochemical staining for F4/80 (A, upper panel) and MPO (A, lower panel) in liver tissue from the control, model, low-dose ATG-treatment, and high-dose ATG-treatment groups (scale bar: 50 μm), along with the quantification of F4/80 (B) and MPO (C) in liver tissue. (D–H) Relative mRNA expressions of cytokines and chemokines, including CCL2 (D), CXCL1 (E), CXCL15 (F), CXCL5 (G), and CXCL3 (H) in liver tissue from four groups were measured using RT-qPCR. Normalized against 18S. (I–K) Levels of MDA (I), CAT (J), and SOD (K) of liver tissue from four groups were measured using RT-qPCR. Normalized against 18S. Data are presented as mean \pm SEM. *p < 0.05, **p < 0.01, ****p < 0.001, ***p < 0.001, ***p < 0.001, ***p < 0.001, ***p

antioxidant gene (nuclear factor erythroid 2-related factor 2) and downregulated levels of pro-oxidant genes (cytochrome B-245 alpha chain and NADPH oxidase 2) (Fig. 2L–N), further confirming the ameliorating effect of ATG on liver oxidative stress. This may be a downstream mechanism of reduced inflammation. These results indicated that ATG improved MASH progression by reducing inflammatory cell infiltration and preventing inflammation-induced oxidative stress.

ATG ameliorated liver fibrogenesis in MASH

Fibrosis is an indicator of disease severity. First, we performed Sirius red and Masson's trichrome staining to evaluate collagen deposition (Fig. 3A-C). We found that eight-week CDAH-FD dietary administration resulted in the formation of fibrous cords with some bridging areas. In contrast, ATG prophylaxis reduced collagen accumulation in a dose-dependent manner (Fig. 3A-C). Immunohistochemical analysis of α-SMA, a marker of activated hepatic stellate cells (HSCs) and fibrosis progression, provided additional confirmation. The a-SMA expression was markedly elevated in the model group but significantly attenuated in the ATG-treated groups (Fig. 3A and D). To further explore the anti-fibrotic effects of ATG, we assessed the expression levels of fibrosis-related genes, including a-SMA, transforming growth factor-beta, vimentin, collagen I, collagen II, and collagen III. The expression of these genes was considerably elevated in the model group compared to the control group, whereas ATG treatment markedly suppressed their expression (Fig. 3E-J). Collectively, these results suggested that ATG mitigated fibrosis in the CDAHFD-induced MASH model, potentially by reducing inflammation.

ATG targeted the NLRP3 inflammasome pathway in macrophages

The chemical structure of ATG is shown in Figure 4A. Using Swiss Target Prediction, the PharmMapper database, the Similarity Ensemble Approach, and relevant literature, we identified 177 potential targets for ATG (Fig. 4B). Among these, 49 therapeutic targets were identified by intersecting the predicted ATG targets with 1,391 MAFLD-related targets obtained from the Genetic Association Database (Fig. 4C and D). To investigate the relationships between these targets, we created a protein-protein interaction network (Fig. 4E). Key nodes in the network include AKT1, PPARG, HSP90AA1, PTGS2, NFkB1, MTOR, and NLRP3, highlighting their potential roles in mediating ATG's effects on MAFLD. Gene Ontology enrichment analysis revealed that ATG-associated targets were involved in critical biological functions, including cellular components, molecular functions, and biological processes (Fig. 4F). Kyoto Encyclopedia of Genes and Genomes pathway analysis identified 201 enriched pathways. The most significant pathways suggested that ATG modulates MAFLD through multiple signaling cascades, including the PI3K-Akt, toll-like receptor, and C-type lectin receptor signaling pathways (Fig. 4G). Reactome pathway enrichment analysis revealed 631 enriched pathways, with the top 20 pathways implicating NLRP3 inflammasome activation as a critical mechanism underlying ATG's therapeutic effects

To further explore the distribution of liver NLRP3 expression in cells and determine the cell types targeted by ATG, we searched the online Liver Cell Atlas and found that NLRP3 was mainly expressed in liver macrophages, monocytes, monocyte-derived cells, and neutrophils (Supplementary Fig. 2A). This finding was further supported by immunofluorescence staining, wherein NLRP3 and CD86 (macrophage

activation markers) co-localized in the liver tissue of CDAH-FD-fed mice, but not in HSCs (Fig. 4I and J and Supplementary Fig. 2B). Importantly, the number of CD86+/NLRP3+ macrophages markedly increased in the model group and significantly decreased following ATG treatment (Fig. 4I and J). There were no alterations in CD206 and ARG1 levels after ATG administration *in vivo* or *in vitro* (Supplementary Fig. 2C-F). These results indicate that ATG exerts its preventive CFF on MASH through complex molecular interactions and signaling pathways, with the NLRP3 inflammasome playing a central role.

Molecular docking analysis performed on the CB-Dock2 server identified potential ligand binding sites and poses for ATG on the NLRP3 receptor (Table 2, Fig. 4K). The optimal Vina score of -7.3 indicates a strong binding affinity between ATG and NLRP3. CETSA coupled with Western blotting in cell lysates (Fig. 4L; Supplementary Fig. 3A) demonstrated significantly enhanced thermal stability of NLRP3 following ATG treatment. Collectively, these findings demonstrate that ATG may exert its biological effects through direct binding to NLRP3.

ATG reduced NLRP3-dependent inflammatory response

To determine the mechanisms by which ATG prevents MASH, we examined the hepatic levels of major inflammatory cytokines and chemokines. mRNA levels of NLRP3, IL-1ß, and tumor necrosis factor-a (TNF-a) were elevated in the model group, but suppressed in both ATG groups (Fig. 5A-C). We investigated the level of activation of the NLRP3 inflammasome complex in liver tissue, as mature IL-1ß indicates inflammasome activation. Western blotting showed that the levels of NLRP3, mature IL-1β, and GSDMD-N proteins were significantly increased in the model group, indicating strong inflammasome activation (Fig. 5D-G; Supplementary Fig. 3B). ATG significantly reduced the levels of these proteins in a dose-dependent manner (Fig. 5D-G). These findings suggest that ATG effectively inhibits macrophage infiltration and pro-inflammatory cytokine expression in CDAHFD-fed mice, primarily by inhibiting the NLRP3 inflammasomes. IL-1β is a central mediator of inflammasome-induced inflammation, and its potent reduction highlights the potential of ATG to modulate the inflammatory environment of MASH.

ATG inhibited the NLRP3-dependent inflammatory response of macrophages in vitro

To determine the anti-inflammatory mechanisms of ATG, we investigated its effects on the NLRP3 inflammasome pathway in macrophages using an in vitro model. RAW264.7 cells were stimulated with LPS to mimic an inflammatory state. ATG treatment (50 and 100 µM) significantly reduced the mRNA expression of key inflammatory markers, including NLRP3, IL-1β, TNF-a, and inducible nitric oxide synthase, in a concentration-dependent manner (Fig. 6B-E). Importantly, ATG had no cytotoxic effects on macrophage viability, even at higher concentrations (Fig. 6A). To investigate the mechanisms underlying NLRP3 transcriptional regulation, we performed cross-database prediction of potential transcription factors for NLRP3. Intersectional analysis of the predicted results identified three candidate transcription factors (Fig. 6F). Further intersection with ATG-associated targets revealed only FOS, a gene encoding the c-Fos protein that acts as a positive regulator of NLRP3 (Fig. 6F). In vitro experiments demonstrated that ATG treatment reduced the nuclear localization of c-Fos while increasing its cytoplasmic accumulation (Fig. 6G-I; Supplementary Fig. 3C).

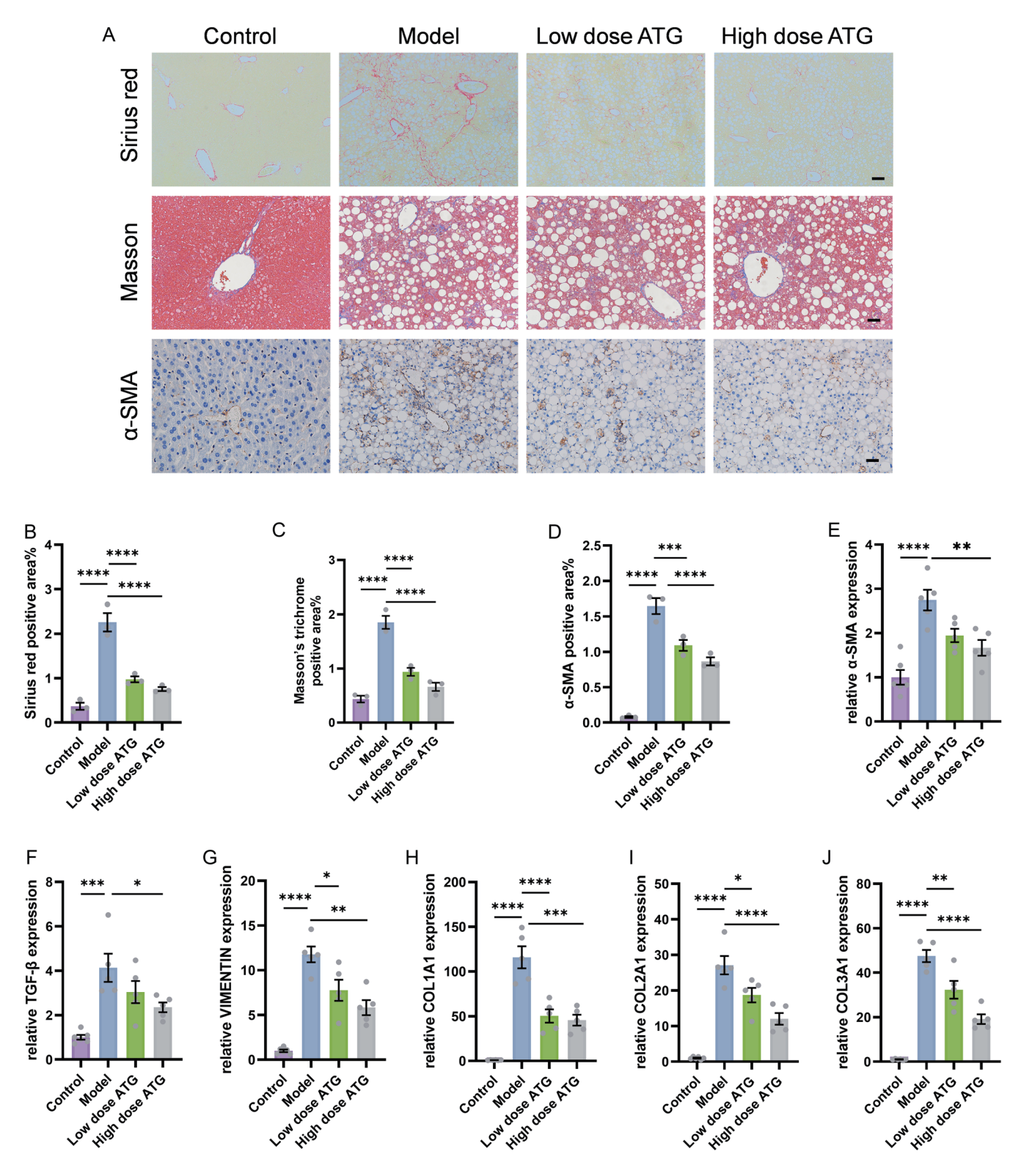


Fig. 3. Effects of ATG on liver fibrosis induced by CDAHFD. (A–D) Sirius red staining (A, upper panel), Masson's trichrome staining (A, middle panel), and immunohistochemical staining for α-SMA expression (A, lower panel) in liver tissue from the control, model, low-dose ATG-treatment, and high-dose ATG-treatment groups (scale bar: 50 μm), along with quantification of each indicator (B–D). (E–J) Relative mRNA levels of fibrosis-related genes, including α-SMA (E), TGF-β (F), VIMENTIN (G), COL1A1 (H), COL2A1 (I), and COL3A1 (J) in the liver tissue from four groups were measured using real-time quantitative polymerase chain reaction. Normalized against 18S. Data are presented as mean ± SEM. *p < 0.05, **p < 0.01, ***p < 0.001, ****p < 0.001. ATG, arctigenin; MASH, metabolic dysfunction-associated steatohepatitis; CDAHFD, choline-deficient, L-amino acid-defined, high-fat diet; SEM, standard error of the mean.

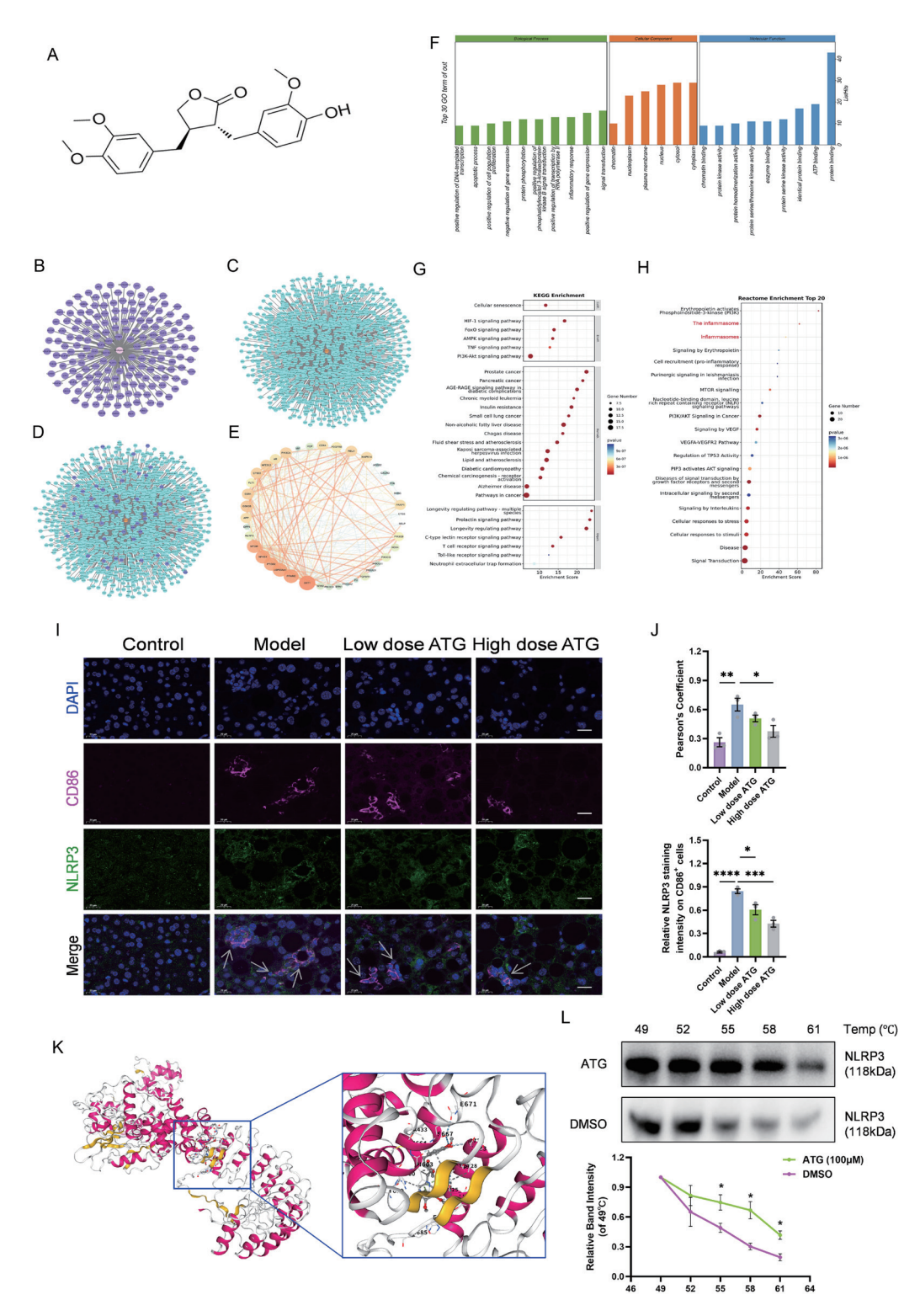


Fig. 4. Target analysis of ATG in MAFLD. (A) Chemical structure of ATG. (B) Target prediction of ATG. (C) Molecular targets associated with MAFLD. (D) Intersection of ATG-specific and MAFLD-related targets. (E) The PPI network of intersection targets between ATG and MAFLD-related targets. (F) GO enrichment analysis of the intersected targets. (G–H) Enrichment of KEGG pathway (G) and Reactome pathway (H) of ATG's targets. (I–J) Immunofluorescence analysis of the colocalization of NLRP3 and CD86 in mice liver from four groups (scale bar: $20 \mu m$), staining intensity was quantified, and colocation analysis was performed. (K) NLRP3 with ATG bound to the cavity. (L) Western blot of CETSA experiment to further confirm the interaction between NLRP3 and ATG in RAW264.7 cells, the temperature ranges from 49°C to 61°C, with relative band intensity normalized to 49°C. Data are presented as mean \pm SEM. *p < 0.05, **p < 0.01, ****p < 0.001, ****p < 0.001. ATG, arctigenin; MAFLD, metabolic dysfunction-associated fatty liver disease; PPI, protein-protein interaction; KEGG, Kyoto Encyclopedia of Genes and Genomes; NLRP3, NLR family pyrin domain containing 3; SEM, standard error of the mean.

Table 2. Molecular docking results of ATG on NLRP3 obtained from the CB-Dock2 server

Curpocket ID	Vina score	Cavity volume (Å3)	Center (x, y, z)	Docking size (x, y, z)	Contact residues
C4	-7.3	1,847	-4, 6, -1	22, 28, 33	Chain A: ARG393 ALA394 ALA395 SER397 LEU398 GLU401 LYS430 SER431 LEU432 ALA433 GLN434 THR659 ARG660 HIS663 MET664 SER667 GLU671 PHE683 HIS685 ASN722 LEU725 THR726 SER728 PHE729 GLY732 LEU733
C1	-7.1	13,545	21, -10, -26	35, 35, 22	Chain A: ILE151 GLU152 ASP153 ARG154 ARG167 ALA227 ALA228 GLY229 ILE230 GLY231 LYS232 THR233 ILE234 ARG237 GLN308 ARG351 TYR381 PRO412 LEU413 TRP416 LEU450 LEU451 GLN452 PRO453 ARG454 GLY455 GLY456 ASP498 VAL499 SER500 ALA501 PHE502
C2	-6.0	3,535	22, -4, -6	30, 30, 22	Chain A: GLU184 LEU188 ALA189 LYS192 THR193 LYS194 THR195 GLU375 ASN402 GLU403 PHE406 THR407 GLY476 ILE477 ASN479 GLN480 LYS481 ILE482 LEU483 PHE484 MET523 GLN526 GLU527 TYR572
C3	-6.0	1,895	-2, -11, 7	22, 22, 22	Chain A: GLU401 ASN402 GLU403 VAL404 TYR565 GLU569 ILE574 PHE575 ARG578 GLN624 PR0625 SER626 GLN627 LEU628 GLU629 TYR632 ASN656 LEU657 SER658 THR659 MET661 ASP662 LEU684 ASN686
C5	-5.9	825	37, -8, -13	22, 22, 22	Chain A: LYS175 GLU176 HIS177 ARG178 SER179 GLN180 ARG183 ASP212 GLN225 PRO352 LEU355 GLN359 PRO365 ARG366 HIS367 GLU369 ARG504 MET505 ASN506 LEU507 PHE508 GLN509 CYS514

ATG, arctigenin; NLRP3, NLR family pyrin domain containing 3.

At the protein level, ATG suppressed the activation of the NLRP3 inflammasome pathway. ATG treatment (20, 50, and 100 μM) markedly inhibited the expression of NLRP3, mature IL-1β, and GSDMD-N, key components of the inflammasome activation cascade (Fig. 6J-M; Supplementary Fig. 3D). In addition, we tested a series of chemokines in vitro and found that the release of chemokines CXCL1, CXCL3, CXCL5, and CXCL15 by RAW264.7 cells decreased after ATG treatment (Fig. 6N-Q), which indirectly suggests that ATG attenuates immune cell infiltration by reducing the release of chemokines by macrophages in mouse models. These results suggest that ATG attenuates macrophage-mediated inflammation by interfering with the NLRP3 inflammasome-dependent signaling pathway. Collectively, these findings demonstrate that ATG suppresses NLRP3-driven inflammatory responses, providing a possible molecular explanation for the anti-inflammatory effects observed in CDAHFD-induced MASH.

Discussion

MASH is a key step in the progression of liver steatosis, and its prominent heterogeneity poses a major challenge in identifying therapeutic targets. Interventional approaches for MASH progression are limited. However, traditional herbal medicines and their multiple pharmacological monomers may provide a potential solution for MASH intervention according to recent studies. 13 The present study revealed, for the first time, that ATG has a preventive effect on CDAHFD-induced MASH by attenuating liver inflammation, oxidative stress, and fibrosis. Based on previous reports and our experiments, hepatic macrophages have been recognized as key drivers of MASH progression. 44-50 NLRP3 expression underlies liver inflammation and fibrosis.51,52 The present study aimed to explore the MASH-preventive actions of the herbal extract ATG, with a dramatic cascade of NLRP3 and inflammasome activation in hepatic macrophages as the underlying molecular mechanisms. The dose-dependent reduction in the NAS score, particularly through amelioration of lobular inflammation, revealed the anti-inflammatory properties of ATG rather than normalization of lipid dysregulation. This finding is supported by the decreased expression of pro-inflammatory cytokines (IL-1 β , TNF-a) and chemokines (C-C motif chemokine 2, CXCL1/3/5/15), which are essential players in recruiting immune cells to impair hepatocytes. $^{53-55}$ Notably, the reduction in CD86⁺/NLRP3⁺ macrophages in ATG-treated mice suggested targeted normalization of macrophage polarization, one of the crucial mechanisms related to the development of steatohepatitis. 56

Inflammation and oxidative stress reinforce each other through a vicious cycle that drives the progression of MAFL to MASH. Activated inflammatory responses in the liver not only impair hepatocytes but also cause ROS overproduction by damaging the mitochondrial respiratory chain. However, oxidation in both steatotic hepatocytes and immune cells (i.e., macrophages and activated neutrophils) can decrease endogenous antioxidants and recruit circulating immune cells to exacerbate hepatic inflammation. Previous studies have demonstrated the safety and tolerability of ATG and its antiinflammatory and antioxidant properties through multiple targets to improve a variety of inflammatory diseases. 57-59 Our group used a CDAHFD to construct a mouse model of MASH. which effectively simulated the characteristics of inflammatory infiltration and oxidative stress in patients with MASH.60 In the current study, we found that the prophylactic use of ATG reduced the expression of multiple hepatic chemokines, attenuated the hepatic infiltration of macrophages and neutrophils, and relieved hepatic oxidative stress. Prophylactic use of ATG has been shown to have an ameliorating effect on MASH through its anti-inflammatory and antioxidant effects.

Mechanistically, ATG significantly reduced the levels of NLRP3, mature IL-1 β , and GSDMD-N in macrophages, indicating that ATG interferes with inflammasome activation to mitigate the macrophage-driven inflammatory response. Unlike its role in inhibiting NLRP3 inflammasome assembly in colon macrophages by downregulating carnitine palmitoyltransferase-1 expression, ¹⁸ ATG employed in our experiments

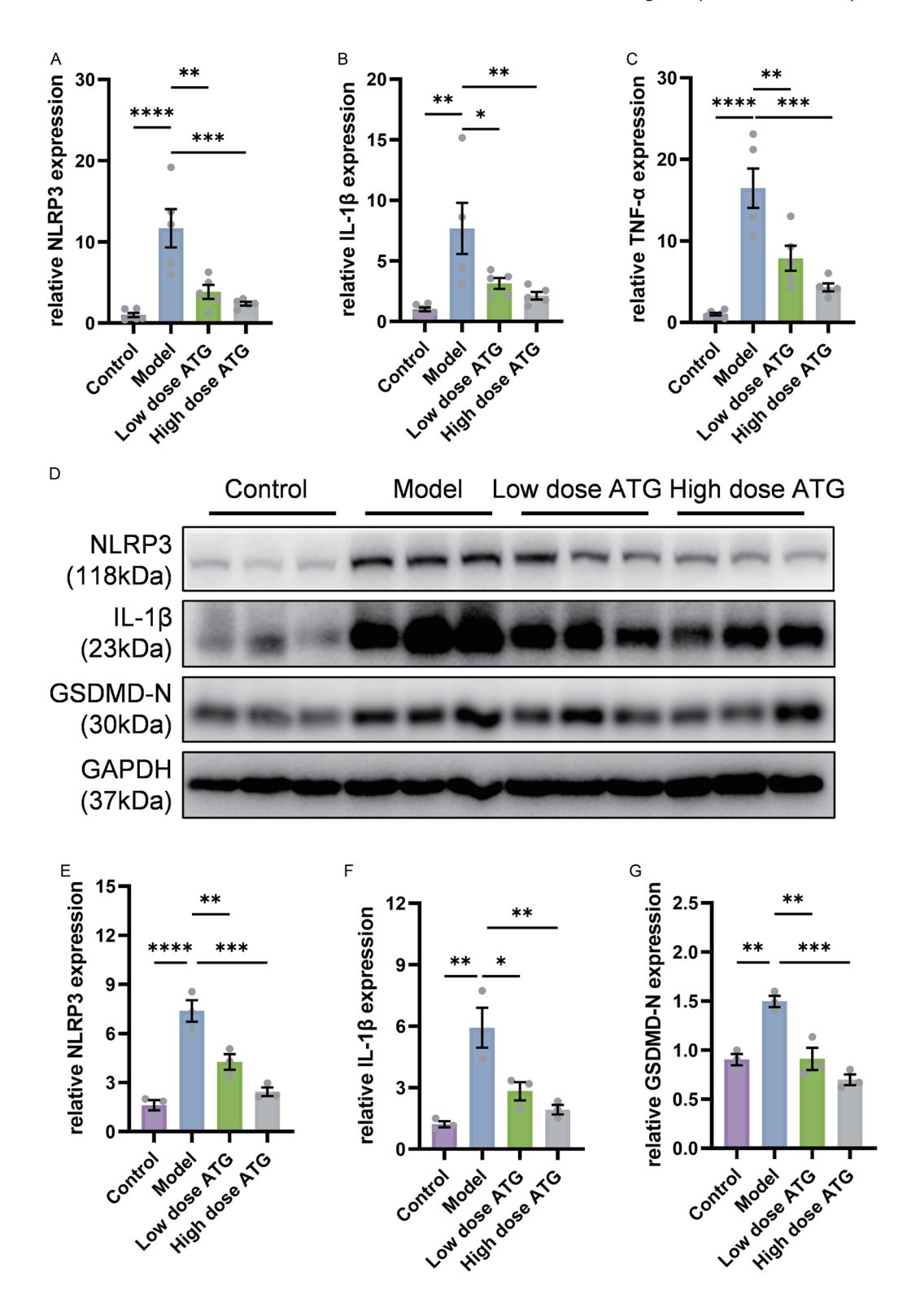


Fig. 5. Effect of ATG on inflammatory response through NLRP3 inflammasome pathway. (A–C) Relative mRNA levels of NLRP3 (A), IL-1 β (B), and TNF- α (C) in liver tissue from four groups were measured using real-time quantitative polymerase chain reaction. Normalized against 18S. (D–G) Western blot (D) and relative protein levels of NLRP3 (E), mature IL-1 β (F), and GSDMD-N (G) in liver tissue from four groups, normalized against GAPDH. Data are presented as the mean \pm SEM. *p < 0.05, **p < 0.01, *****p < 0.001, ******p < 0.0001. ATG, arctigenin; NLRP3, NLR family pyrin domain containing 3; SEM, standard error of the mean; GAPDH, glyceraldehyde-3-phosphate dehydrogenase.

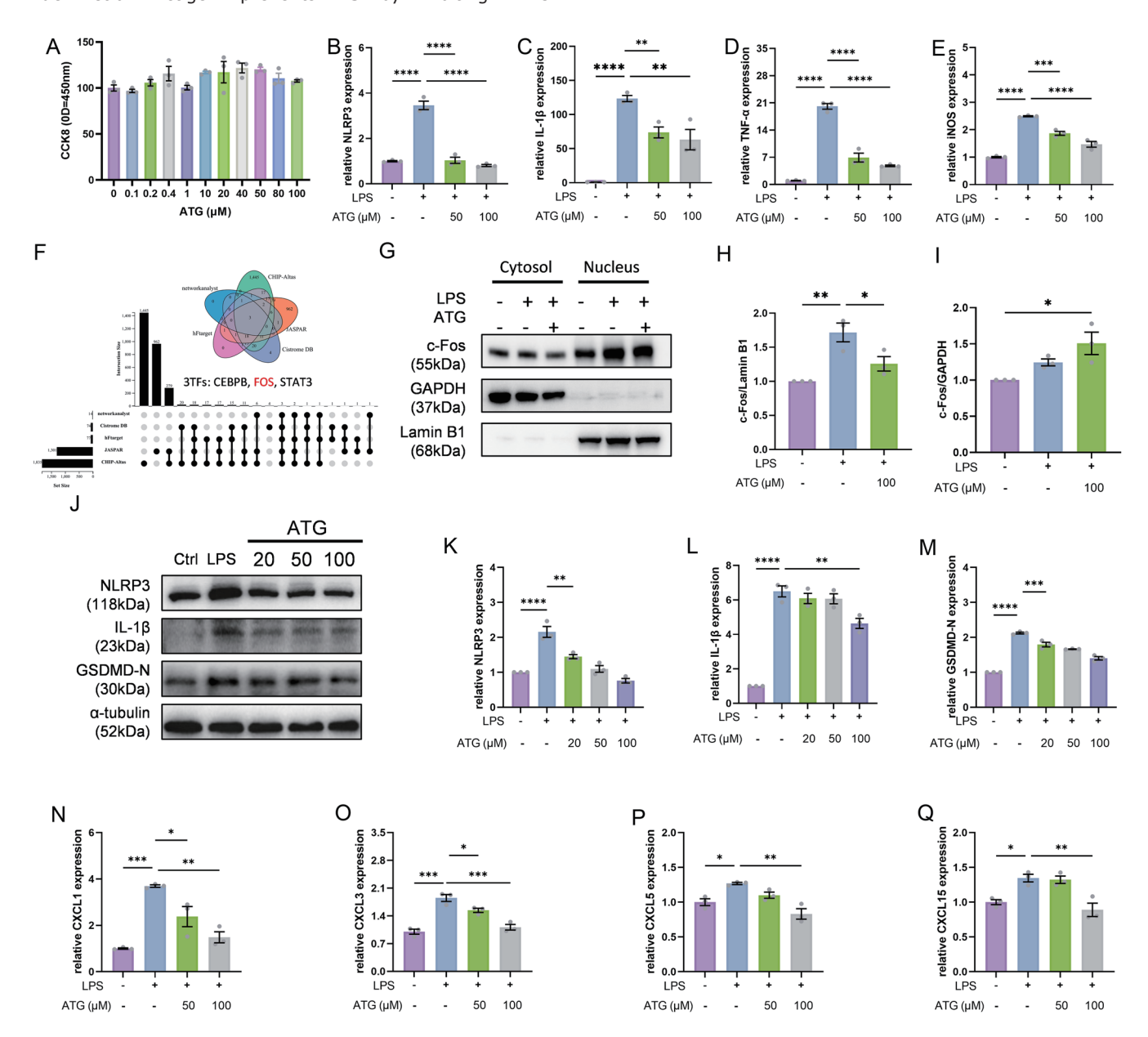


Fig. 6. Effect of ATG on RAW264.7 by regulating NLRP3 inflammasome pathway. (A) Cell viability of RAW264.7 cells after treatment with different concentrations of ATG (0, 0.1, 0.2, 0.4, 1, 10, 20, 40, 50, 80, and 100 μM) for 24 h. (B–E) RT-qPCR was utilized to assess the mRNA expression of NLRP3 (B), IL-1β (C), TNF-α (D), and iNOS (E) of RAW264.7 cells following treatment with LPS in the absence or presence of two concentrations of ATG, along with the Control group. Normalized against 18S. (F) Venn diagram and Upset plot showing the potential transcription factors of NLRP3 predicted by different databases. (G–I) Western blot was utilized to assess the cytosol and nucleus protein level of C-FOS in RAW264.7 cells following treatment with LPS in the absence or presence of ATG, along with the Control group. Normalized against GAPDH and Lamin B1, separately. (J–M) Western blot was utilized to assess the protein level of NLRP3 (K), mature IL-1β (L), and GSDMD-N (M) of RAW264.7 cells following treatment with LPS in the absence or presence of three concentrations of ATG, along with the Control group. Normalized against a-tubulin. (N–Q) RT-qPCR was utilized to assess the mRNA expression of CXCL1 (N), CXCL3 (O), CXCL5 (P), and CXCL15 (Q) of RAW264.7 cells following treatment with LPS in the absence or presence of two concentrations of ATG, along with the Control group. Normalized against 18S. Data are presented as mean ± SEM. *p < 0.05, **p < 0.01, ****p < 0.001, ****p < 0.00

demonstrated that it inhibited the transcription of NLRP3 in macrophages by decreasing the nuclear translocation of c-Fos. Molecular docking (-7.3 Vina score) and cellular CET-SA analyses confirmed that ATG directly bound to NLRP3. Collectively, ATG may inhibit the expression and function of NLRP3, thus attenuating the secretion of NLRP3-dependent inflammatory cytokines and chemokines, thereby disrupting the positive feedback loop of immune cell recruitment. This

is consistent with evidence that activation of NLRP3 in macrophages exacerbates hepatic inflammation. 45,61

Studies have demonstrated that excessive lipid species (e.g., cholesterol, ceramides) activate NLRP3 by inducing organelle stress, thus accelerating the inflammatory response. 62,63 As for the effect of NLRP3 on lipid metabolism during diabetic nephropathy, MCC950, a NLRP3-specific inhibitor, ameliorates podocyte lipid accumulation by promot-

ing ATP-binding cassette A1 expression and inhibiting both sterol regulatory element-binding protein 1 and 2.64 There are also experiments focusing on MCC950-based NLRP3 inhibition in MAFLD. With little impact on hepatic lipid metabolism, MCC950 inhibits inflammatory cell infiltration, thereby improving hepatocyte injury, lobular inflammation, and liver fibrosis.⁵⁶ This inconsistency indicates the diverse effects of NLRP3 on lipid metabolism across different diseases and models. In our experiments, serum levels of FFA and VLDL, together with hepatic content of TG and hepatocyte steatosis, demonstrated a significant increase during CDAHFD modeling. However, these indices experienced limited alteration after ATG intervention. Similarly, there were no statistical differences in the expression of key genes related to FFA, VLDL, cholesterol, and ceramide metabolism upon ATG administration. These results were consistent with findings reported by AR et al.,56 suggesting an inflammation-rather than metabolism-based pharmacological action of ATG.

The anti-fibrotic effect of ATG has been reflected by reduced collagen deposition and a-SMA expression, possibly due to the aforementioned inhibition of inflammatory pathways. In MASH, the resolution of fibrosis is usually due to a decrease in hepatocyte damage and inflammatory signaling. This premise is further supported by the down-regulation of transforming growth factor-beta and collagen-related genes, as persistent inflammation directly activates HSCs, promoting extracellular matrix remodeling. Although our study did not directly assess HSC activation, the simultaneous reduction in NLRP3-driven markers of inflammation and fibrosis suggested an indirect mechanism, consistent with reports linking NLRP3 inhibition to HSC deactivation.

Given the critical actions of macrophages in MASH and related liver fibrosis/cirrhosis, macrophage NLRP3 also serves as a potential target for therapy. Studies of selective NLRP3 inhibitors have shown that NLRP3 inactivation has therapeutic effects on MASH. For instance, in vivo administration of the selective NLRP3 inhibitor MCC950 significantly attenuated hepatocyte injury, lobular inflammation, and liver fibrosis in mice with both MASH and chronic ethanol abuse. 65 In another study of rodent MASH induced by an atherogenic diet, a four-week intervention of MCC950 improved liver enzymes. After eight weeks of treatment, reductions were observed in the NAS score, infiltration of macrophages and neutrophils, as well as liver inflammation and fibrosis. 56 Therefore, we speculate that ATG is likely to possess therapeutic potential in MASH through transcriptional and functional inactivation of NLRP3. When compared to ATG, MCC950 specifically targets inflammasome assembly without suppressing transcriptional activation.⁶⁸ Moreover, clinical trials have revealed elevated levels of liver enzymes associated with MCC950 administration, indicating drug-induced hepatotoxicity.⁶⁹ Another selective inhibitor, CY-09, directly binds to the ATP-binding domain of NLRP3, thereby inhibiting ATPase activity and subsequent inflammasome activation, with no effect on other pro-inflammatory signaling pathways. 70 In contrast, ATG exhibits multitarget anti-inflammatory mechanisms without reported drug toxicity,71 even at doses of 30-120 mg/kg in the present experiments.

Intertwined metabolic and inflammatory abnormalities have been well established as underlying factors in MASH. In our experiments, it is worth noting that the pharmacological effect of ATG on MASH primarily occurs through dosedependent reduction in inflammation. The mild effect of ATG on MASH-related dysregulation of lipid metabolism reflects the limitations of this study, and its safety needs to be verified in a long-term model. Recent studies have shown that

PPARa improves lipid metabolism, partially by accelerating fatty acid oxidation, to attenuate hepatic lipid accumulation. Administration of PPARa agonists, such as fenofibrate and pemafibrate, demonstrates reliable improvements in the hepatic lipid profile and, consequently, liver function. Thus, a combination of ATG and PPARa agonists could be a better choice for the prevention and/or treatment of MASH through their synergistic effects on both metabolic and inflammatory abnormalities.

Conclusions

ATG may prevent CDAHFD-induced MASH primarily by suppressing the NLRP3/GSDMD-N axis in macrophages, thereby attenuating inflammation, oxidative stress, and fibrosis, with a mild effect on lipid dysmetabolism. These findings suggest that ATG is a promising candidate for MASH treatment, particularly in the context of the unmet therapeutic needs for inflammation-driven fibrosis. However, further studies are needed to explore the synergistic effects of ATG and lipid-lowering therapy to fully exploit their metabolic and inflammatory regulatory potential.

Funding

This work was supported by the Noncommunicable Chronic Diseases-National Science and Technology Major Project, No. 2023ZD0508700; and the National Natural Science Foundation of China, No. 82170593, 82170588.

Conflict of interest

JGF has been an Associate Editor of the *Journal of Clinical* and *Translational Hepatology* since 2013. The other authors have no conflicts of interest related to this publication.

Author contributions

Mouse keeping and husbandry (RX, TYR, QJW, QRZ), carrying out of experiments and data analysis (RX, LJ, QJW, QRZ), conceptualization and design of the study (QP, JGF), manuscript preparation (RX, TYR, RXY, QP, JGF), and supervision of the study (QP, JGF). All authors read and approved the final version and publication of the manuscript.

Ethical statement

All animal handling and experimental procedures were approved by the Animal Care and Use Committee of Xinhua Hospital Affiliated to Shanghai Jiao Tong University School of Medicine (Approval No. XHEC-NSFC-2023-273). All animals received humane care.

Data sharing statement

No additional data are available.

References

- [1] Fan JG, Xu XY, Yang RX, Nan YM, Wei L, Jia JD, et al. Guideline for the Prevention and Treatment of Metabolic Dysfunction-associated Fatty Liver Disease (Version 2024). J Clin Transl Hepatol 2024;12(11):955–974. doi:10.14218/JCTH.2024.00311, PMID:39544247.
- [2] Vitale A, Svegliati-Baroni G, Ortolani A, Cucco M, Dalla Riva GV, Giannini EG, et al. Epidemiological trends and trajectories of MAFLD-associated hepatocellular carcinoma 2002-2033: the ITA.LI.CA database. Gut

- 2023;72(1):141-152. doi:10.1136/gutjnl-2021-324915, PMID:34933916. Kazankov K, Jørgensen SMD, Thomsen KL, Møller HJ, Vilstrup H, George J, et al. The role of macrophages in nonalcoholic fatty liver disease and nonalcoholic steatohepatitis. Nat Rev Gastroenterol Hepatol 2019;16(3):145–159. doi:10.1038/s41575-018-0082-x, PMID:30482910.
 Tacke F. Targeting hepatic macrophages to treat liver diseases. J Hepa-
- tol 2017;66(6):1300-1312. doi:10.1016/j.jhep.2017.02.026, PMID:282
- Karkanitsa M, Sadtler K. Early factors in the immune response to biomaterials. Immunomodulatory Biomaterials. Philadelphia, PA: Elsevier; 2021:25– [5]
- Miura K, Yang L, van Rooijen N, Ohnishi H, Seki E. Hepatic recruitment [6] of macrophages promotes nonalcoholic steatohepatitis through CCR2. Am J Physiol Gastrointest Liver Physiol 2012;302(11):G1310-G1321.
- doi:10.1152/ajpgi.00365.2011, PMID:22442158.

 Mridha AR, Haczeyni F, Yeh MM, Haigh WG, Ioannou GN, Barn V, et al. TLR9 is up-regulated in human and murine NASH: pivotal role in inflammatory recruitment and cell survival. Clin Sci (Lond) 2017;131(16):2145–2159. doi:10.1042/CS20160838, PMID:28687713.
- Novo E, Cappon A, Villano G, Quarta S, Cannito S, Bocca C, et al. SerpinB3 as a Pro-Inflammatory Mediator in the Progression of Experimental Non-Alcoholic Fatty Liver Disease. Front Immunol 2022;13:910526. doi:10.3389/fimmu.2022.910526, PMID:35874657.
- Chatterjee S, Ganini D, Tokar EJ, Kumar A, Das S, Corbett J, et al. Leptin is key to peroxynitrite-mediated oxidative stress and Kupffer cell activation in experimental non-alcoholic steatohepatitis. J Hepatol 2013;58(4):778–784. doi:10.1016/j.jhep.2012.11.035, PMID:23207144. [10] Huang W, Metlakunta A, Dedousis N, Zhang P, Sipula I, Dube JJ, et al.
- Depletion of liver Kupffer cells prevents the development of diet-induced hepatic steatosis and insulin resistance. Diabetes 2010;59(2):347–357.
- hepatic steatosis and insulin resistance. Diabetes 2010;59(2):347–357. doi:10.2337/db09-0016, PMID:19934001.

 [11] Wang C, Ma C, Gong L, Guo Y, Fu K, Zhang Y, et al. Macrophage Polarization and Its Role in Liver Disease. Front Immunol 2021;12:803037. doi:10.3389/fimmu.2021.803037, PMID:34970275.

 [12] Yang B, Luo W, Wang M, Tang Y, Zhu W, Jin L, et al. Macrophage-specific MyD88 deletion and pharmacological inhibition prevents liver damage in non-alcoholic fatty liver disease via reducing inflammatory response. Biochim Biophys Acta Mol Basis Dis 2022;1868(10):166480. doi:10.1016/j. bhadis 2022 166480. PMID:35811033. bbadis.2022.166480, PMID:35811033.
- [13] Cao Y, Fang X, Sun M, Zhang Y, Shan M, Lan X, et al. Preventive and therapeutic effects of natural products and herbal extracts on nonal-coholic fatty liver disease/nonalcoholic steatohepatitis. Phytother Res 2023;37(9):3867–3897. doi:10.1002/ptr.7932, PMID:37449926.
- [14] Huang SL, Yu RT, Gong J, Feng Y, Dai YL, Hu F, et al. Arctigenin, a natural compound, activates AMP-activated protein kinase via inhibition of mitochondria complex I and ameliorates metabolic disorders in ob/ob mice. Diabetologia 2012;55(5):1469-1481. doi:10.1007/s00125-011-2366-3, PMID:22095235.
- [15] Hyam SR, Lee IA, Gu W, Kim KA, Jeong JJ, Jang SE, et al. Arctigenin ameliorates inflammation in vitro and in vivo by inhibiting the PI3K/AKT pathway and polarizing M1 macrophages to M2-like macrophages. Eur J Pharmacol 2013;708(1-3):21–29. doi:10.1016/j.ejphar.2013.01.014, PMID:233 75038
- [16] Zhong Y, Lee K, Deng Y, Ma Y, Chen Y, Li X, et al. Arctigenin attenuates diabetic kidney disease through the activation of PP2A in podocytes. Nat Commun 2019;10(1):4523. doi:10.1038/s41467-019-12433-w, PMID:315
- [17] Chen KY, Lin JA, Yao HY, Hsu AC, Tai YT, Chen JT, et al. Arctigenin pro-tects against steatosis in WRL68 hepatocytes through activation of phosphoinositide 3-kinase/protein kinase B and AMP-activated protein kinase pathways. Nutr Res 2018;52:87–97. doi:10.1016/j.nutres.2018.02.004, . PMID:29525610.
- PMID: 29925610.
 [18] Qiao S, Lv C, Tao Y, Miao Y, Zhu Y, Zhang W, et al. Arctigenin disrupts NLRP3 inflammasome assembly in colonic macrophages via downregulating fatty acid oxidation to prevent colitis-associated cancer. Cancer Lett 2020;491:162–179. doi:10.1016/j.canlet.2020.08.033, PMID:32861708.
 [19] Wang ZX, Wang MY, Yang RX, Zhao ZH, Xin FZ, Li Y, et al. Ammonia Scavenger Restores Liver and Muscle Injury in a Mouse Model of Non-alcobolic Staatobapatitis With Sarropapis Oberity. Eront Nutr. 2022;9:898407.
- holic Steatohepatitis With Sarcopenic Obesity. Front Nutr 2022;9:808497. doi:10.3389/fnut.2022.808497, PMID:35369074. [20] Uchida K, Urabe K, Naruse K, Ogawa Z, Mabuchi K, Itoman M. Hyperlipidemia and hyperinsulinemia in the spontaneous osteoarthritis mouse
- model, STR/Ort. Exp Anim panim.58.181, PMID:19448342 2009;58(2):181-187. doi:10.1538/ex
- [21] Qiu F, Long H, Zhang L, Liu J, Yang Z, Huang X. Dermcidin Enhances the Migration, Invasion, and Metastasis of Hepatocellular Carcinoma Cells In Vitro and In Vivo. J Clin Transl Hepatol 2022;10(3):429–438. doi:10.14218/JCTH.2021.00108, PMID:35836774.
 [22] Zhang QR, Zhang JB, Shen F, Xue R, Yang RX, Ren TY, et al. Loss of NAT10 and Control of the Con
- alleviates maternal high-fat diet-induced hepatic steatosis in male offspring of mice. Obesity (Silver Spring) 2024;32(7):1349–1361. doi:10.1002/oby.24041, PMID:38816990. [23] Zhang J, Jiang D, Lin S, Cheng Y, Pan J, Ding W, et al. Prolyl endopeptidase
- disruption reduces hepatic inflammation and oxidative stress in methionine-choline-deficient diet-induced steatohepatitis. Life Sci 2021;270:119131.
- doi:10.1016/j.lfs.2021.119131, PMID:33516698.

 [24] Zou ZY, Ren TY, Li JQ, Jiao TY, Wang MY, Huang LJ, et al. Transcriptomic Landscape Analysis Reveals a Persistent DNA Damage Response in Metabolic Dysfunction-associated Steatohepatitis Post-dietary Intervention. J Clin Transl Hepatol 2024;12(9):765-779. doi:10.14218/JCTH.2024.00111, PMID:39280071.

- [25] Takahashi Y, Fukusato T. Histopathology of nonalcoholic fatty liver disease/
- [25] Takariasin Y, Fukusato I. Riscopatiology of Indiraction and College Ponnal Coholic Steatohepatitis. World J Gastroenterol 2014;20(42):15539–15548. doi:10.3748/wjg.v20.i42.15539, PMID:25400438.
 [26] Harms PW, Frankel TL, Moutafi M, Rao A, Rimm DL, Taube JM, et al. Multiplex Immunohistochemistry and Immunofluorescence: A Practical Update for Pathologists. Mod Pathol 2023;36(7):100197. doi:10.1016/j.modpat.2023.100197, PMID:37105494.
- [27] Livak KJ, Schmittgen TD. Analysis of relative gene expression data using real-time quantitative PCR and the 2(-Delta Delta C(T)) Method. Methods 2001;25(4):402–408. doi:10.1006/meth.2001.1262, PMID:11846609.
- [28] Stiekemà M, Ramaekers FCS, Kapsokalyvas D, van Zandvoort MAMJ, Vel-trop RJA, Broers JLV. Super-Resolution Imaging of the A- and B-Type Lamin Networks: A Comparative Study of Different Fluorescence Labeling Procedures. Int J Mol Sci 2021;22(19):10194. doi:10.3390/ijms221910194,
- PMID:34638534.
 [29] Wang X, Shen Y, Wang S, Li S, Zhang W, Liu X, et al. PharmMapper 2017 update: a web server for potential drug target identification with a comprehensive target pharmacophore database. Nucleic Acids Res 2017;45(W1):W356-W360. doi:10.1093/nar/gkx374, PMID:28472422.
- [30] Keiser MJ, Roth BL, Armbruster BN, Ernsberger P, Irwin JJ, Shoichet BK. Relating protein pharmacology by ligand chemistry. Nat Biotechnol
- 2007;25(2):197–206. doi:10.1038/nbt1284, PMID:17287757.

 [31] Daina A, Michielin O, Zoete V. SwissTargetPrediction: updated data and new features for efficient prediction of protein targets of small molecules. Nucleic Acids Res 2019;47(W1):W357–W364. doi:10.1093/nar/gkz382, PMID:31106366.
- [32] Szklarczyk D, Kirsch R, Koutrouli M, Nastou K, Mehryary F, Hachilif R, et al. The STRING database in 2023: protein-protein association networks and functional enrichment analyses for any sequenced genome of interest. Nucleic Acids Res 2023;51(D1):D638–D646. doi:10.1093/nar/gkac1000, PMID: 36370105.
- [33] Remmerie A, Martens L, Thoné T, Castoldi A, Seurinck R, Pavie B, et al. Osteopontin Expression Identifies a Subset of Recruited Macrophages Distinct from Kupffer Cells in the Fatty Liver. Immunity 2020;53(3):641–657.e14.
- doi:10.1016/j.immuni.2020.08.004, PMID:32888418.
 [34] Liu Y, Cao Y. Protein-Ligand Blind Docking Using CB-Dock2. Methods Mol Biol 2024;2714:113–125. doi:10.1007/978-1-0716-3441-7_6, PMID:376 76595.
- [35] Rauluseviciute I, Riudavets-Puig R, Blanc-Mathieu R, Castro-Mondragon JA, Ferenc K, Kumar V, et al. JASPAR 2024: 20th anniversary of the openaccess database of transcription factor binding profiles. Nucleic Acids Res
- 2024;52(D1):D174-D182. doi:10.1093/nar/gkad1059, PMID:37962376. [36] Oki S, Ohta T, Shioi G, Hatanaka H, Ogasawara O, Okuda Y, *et al.* ChIP-Atlas: a data-mining suite powered by full integration of public ChIP-seq data. EMBO Rep 2018;19(12):e46255. doi:10.15252/embr.201846255, PMID:30413482
- [37] Zheng R, Dong X, Wan C, Shi X, Zhang X, Meyer CA. Cistrome Data Browser and Toolkit: analyzing human and mouse genomic data using compendia of ChIP-seq and chromatin accessibility data. Quant Biol 2020;8(3):267-
- 276. doi:10.1007/s40484-020-0204-7.
 [38] Zhang Q, Liu W, Zhang HM, Xie GY, Miao YR, Xia M, et al. hTFtarget: A Comprehensive Database for Regulations of Human Transcription Factors
- Comprehensive Database for Regulations of Human Transcription Factors and Their Targets. Genomics Proteomics Bioinformatics 2020;18(2):120–128. doi:10.1016/j.gpb.2019.09.006, PMID:32858223.

 [39] Zhou G, Soufan O, Ewald J, Hancock REW, Basu N, Xia J. NetworkAnalyst 3.0: a visual analytics platform for comprehensive gene expression profiling and meta-analysis. Nucleic Acids Res 2019;47(W1):W234–W241. doi:10.1093/nar/gkz240, PMID:30931480.

 [40] Kurien BT, Scofield RH. Western blotting. Methods 2006;38(4):283–293. doi:10.1016/j.ymeth.2005.11.007, PMID:16483794.

 [41] Chen CC, Xie XM, Zhao XK, Zuo S, Li HY. Krüppel-like Factor 13 Promotes HCC Progression by Transcriptional Regulation of HMGCS1-mediated Cholesterol Synthesis. J Clin Transl Hepatol 2022;10(6):1125–1137. doi:10.14218/JCTH.2021.00370. PMID:36381108.

- doi:10.14218/JCTH.2021.00370, PMID:36381108.

 [42] Guo Q, Wu Z, Wang K, Shi J, Wei M, Lu B, et al. Forsythiaside-A improved bile-duct-ligation-induced liver fibrosis in mice: The involvement of alleviating mitochondrial damage and ferroptosis in hepatocytes via activating Nrf2. Free Radic Biol Med 2024;222:27–40. doi:10.1016/j.freeradbiomed.2024.05.042, PMID:38815774.
- [43] Huang X, Yan J, Zhang M, Wang Y, Chen Y, Fu X, et al. Targeting Epigenetic Crosstalk as a Therapeutic Strategy for EZH2-Aberrant Solid Tumors. Cell 2018;175(1):186–199.e19. doi:10.1016/j.cell.2018.08.058, PMID: 30220457.
- [44] Martinon F, Burns K, Tschopp J. The inflammasome: a molecular platform triggering activation of inflammatory caspases and processing of proII-beta. Mol Cell 2002;10(2):417–426. doi:10.1016/s1097-2765(02)00599-3, PMID:12191486
- [45] Kaufmann B, Kui L, Reca A, Leszczynska A, Kim AD, Booshehri LM, et al. Cell-specific Deletion of NLRP3 Inflammasome Identifies Myeloid Cells as Key Drivers of Liver Inflammation and Fibrosis in Murine Steatohepatitis. Cell Mol Gastroenterol Hepatol 2022;14(4):751–767. doi:10.1016/j.
- jcmgh.2022.06.007, PMID:35787975. [46] Li XY, Ji PX, Ni XX, Chen YX, Sheng L, Lian M, *et al.* Regulation of PPAR- γ activity in lipid-laden hepatocytes affects macrophage polarization and inflammation in nonalcoholic fatty liver disease. World J Hepatol
- tion and inflammation in nonalconolic fatty liver disease. World J Hepatol 2022;14(7):1365–1381. doi:10.4254/wjh.v14.i7.1365, PMID:36158922. [47] Yang L, Liu S, He Y, Gan L, Ni Q, Dai A, et al. Exosomes regulate SIRT3-related autophagy by delivering miR-421 to regulate macrophage polarization and participate in OSA-related NAFLD. J Transl Med 2024;22(1):475. doi:10.1186/s12967-024-05283-8, PMID:38764033
- [48] Sun K, Wang J, Lan Z, Li L, Wang Y, Li A, et al. Sleeve Gastroplasty

- Combined with the NLRP3 Inflammasome Inhibitor CY-09 Reduces Body Weight, Improves Insulin Resistance and Alleviates Hepatic Steatosis ir Mouse Model. Obes Surg 2020;30(9):3435–3443. doi:10.1007/s11695-
- Mouse Model. Obes Surg 2020;30(9):3453-3443. doi:10.1007/311033-020-04571-8, PMID:32266697.

 [49] Yang M, Zhao L. The Selective NLRP3-Inflammasome Inhibitor CY-09 Ameliorates Kidney Injury in Diabetic Nephropathy by Inhibiting NLRP3- inflammasome Activation. Curr Med Chem 2023;30(28):3261-3270. doi:10.217 4/0929867329666220922104654, PMID:36154582
- [50] Negro R, Mastrogiacomo R, Carríeri L, Rizzi F, Arrè V, Minervini G, et al. Encapsulation of MCC950 in Liposomes Decorated with Anti-Frizzled 1 Improves Drug Bioavailability and Effectiveness in Fatty Liver Disease. ACS Appl Mater Interfaces 2023;15(28):33322–33334. doi:10.1021/acsami.3c04206, PMID:37417887.

 [51] Inzaugarat ME, Johnson CD, Holtmann TM, McGeough MD, Trautwein C, Papouchado BG, et al. NLR Family Pyrin Domain-Containing 3 Inflammasome Activation in Hepatic Stellate Cells Induces Liver Fibrosis in Mice. Hepatol-
- ogy 2019;69(2):845–859. doi:10.1002/hep.30252, PMID:30180270.
 [52] Wree A, McGeough MD, Peña CA, Schlattjan M, Li H, Inzaugarat ME, et al. NLRP3 inflammasome activation is required for fibrosis development in NAFLD. J Mol Med (Berl) 2014;92(10):1069-1082. doi:10.1007/s00109-014-1170-1, PMID:24861026.
- [53] Herrero-Cervera A, Soehnlein O, Kenne E. Neutrophils in chronic inflammatory diseases. Cell Mol Immunol 2022;19(2):177–191. doi:10.1038/s41423-021-00832-3, PMID:35039631.
 [54] Tacke F, Puengel T, Loomba R, Friedman SL. An integrated view of anti-
- [54] Tacke F, Puengel T, Loomba R, Friedman SL. An integrated view of antitinflammatory and antifibrotic targets for the treatment of NASH. J Hepatol 2023;79(2):552–566. doi:10.1016/j.jhep.2023.03.038, PMID:37061196.
 [55] Wallace SJ, Tacke F, Schwabe RF, Henderson NC. Understanding the cellular interactome of non-alcoholic fatty liver disease. JHEP Rep 2022;4(8):100524. doi:10.1016/j.jhepr.2022.100524, PMID:35845296.
 [56] Mridha AR, Wree A, Robertson AAB, Yeh MM, Johnson CD, Van Rooyen DM, et al. NLRP3 inflammasome blockade reduces liver inflammation and fibrosis in experimental NASH in mice. J Heastel 2012;56(S):1037-1046.
- fibrosis in experimental NASH in mice. J Hepatol 2017;66(5):1037–1046 doi:10.1016/j.jhep.2017.01.022, PMID:28167322.
- [57] Zeng M, Xie Z, Zhang J, Li S, Wu Y, Yan X. Arctigenin Attenuates Vascular Inflammation Induced by High Salt through TMEM16A/ESM1/VCAM-1 Pathway. Biomedicines 2022;10(11):2760. doi:10.3390/biomedicines10112760, PMID:36359280.
 [58] Xiong B, Yang C, Yang X, Luo S, Li S, Chen C, et al. Arctigenin derivations of the pathological manifestations.
- tive A-1 ameliorates motor dysfunction and pathological manifestations in SOD1(G93A) transgenic mice via the AMPK/SIRT1/PGC-1a and AMPK/ SIRT1/IL-1β/NF-κB pathways. CNS Neurosci Ther 2024;30(6):e14692. doi:10.1111/cns.14692, PMID:38872258.
- doi:10.1111/cns.14692, PMID:3887/2258.
 [59] Wang N, Li C, Zhang Z. Arctigenin ameliorates high-fat diet-induced metabolic disorders by reshaping gut microbiota and modulating GPR/HDAC3 and TLR4/NF-kB pathways. Phytomedicine 2024;135:156123. doi:10.1016/j.phymed.2024.156123, PMID:39396403.
 [60] Kisoh K, Sugahara G, Ogawa Y, Furukawa S, Ishida Y, Okanoue T, et al. Estimating Drug Efficacy with a Diet-Induced NASH Model in Chimeric Mice with Humanized Livers. Biomedicines 2021;9(11):1647. doi:10.3390/biomedicines/11.1647. PMID:34829876.
- medicines9111647, PMID:34829876.

- [61] Zhang L, Wang M, An R, Dai J, Liu S, Chen M, et al. Activation of NLRP3 Inflammasome via Drp1 Overexpression in Kupffer Cells Aggravates Ischemia-reperfusion Injury in Hepatic Steatosis. J Clin Transl Hepatol 2023;11(5):1069-1078. doi:10.14218/JCTH.2022.00109, PMID:37577223.
- [62] Liang JJ, Fraser IDC, Bryant CE. Lipid regulation of NLRP3 inflammasome activity through organelle stress. Trends Immunol 2021;42(9):807–823. doi:10.1016/j.it.2021.07.005, PMID:34334306.
- [63] Pizzuto M, Pelegrin P, Ruysschaert JM. Lipid-protein interactions regulating the canonical and the non-canonical NLRP3 inflammasome. Prog Lipid Res 2022;87:101182. doi:10.1016/j.plipres.2022.101182, PMID:35901922.
- 2022;87:101182. doi:10.1016/j.plipres.2022.101182, PMID:35901922.
 [64] Wu M, Yang Z, Zhang C, Shi Y, Han W, Song S, et al. Inhibition of NLRP3 inflammasome ameliorates podocyte damage by suppressing lipid accumulation in diabetic nephropathy. Metabolism 2021;118:154748. doi:10.1016/j.metabol.2021.154748, PMID:33675822.
 [65] Babuta M, Morel C, de Carvalho Ribeiro M, Calenda C, Ortega-Ribera M, Thevkar Nagesh P, et al. Neutrophil extracellular traps activate hepatic stellate cells and monocytes via NLRP3 sensing in alcohol-induced acceleration of MASH fibrosis. Gut 2024;73(1):1854–1869. doi:10.1136/
- celeration of MASH fibrosis. Gut 2024;73(11):1854-1869. doi:10.1136/gutjnl-2023-331447, PMID:38777573.
- [66] Tsuchida T, Friedman SL. Mechanisms of hepatic stellate cell activation. Nat Rev Gastroenterol Hepatol 2017;14(7):397-411. doi:10.1038/nrgas-
- tro.2017.38, PMID:28487545.

 [67] Taru V, Szabo G, Mehal W, Reiberger T. Inflammasomes in chronic liver disease: Hepatic injury, fibrosis progression and systemic inflammation. J Hepatol 2024;81(5):895–910. doi:10.1016/j.jhep.2024.06.016, PMID:38908436.
- [68] Li H, Guan Y, Liang B, Ding P, Hou X, Wei W, et al. Therapeutic potential of MCC950, a specific inhibitor of NLRP3 inflammasome. Eur J Pharmacol 2022;928:175091. doi:10.1016/j.ejphar.2022.175091. PMID:35714692.
 [69] Zheng Y, Zhang X, Wang Z, Zhang R, Wei H, Yan X, et al. MCC950 as a promising candidate for blocking NLRP3 inflammasome activation: A review of preclinical research and future directions. Arch Pharm (Weinheim) 2024;357(41):2400469. doi:10.1003/srds.2024069. PMID:2019.03206
- 2024;357(11):e2400459. doi:10.1002/ardp.202400459, PMID:39180246.

 [70] Jiang H, He H, Chen Y, Huang W, Cheng J, Ye J, et al. Identification of a selective and direct NLRP3 inhibitor to treat inflammatory disorders. Exp Med 2017;214(11):3219-3238. doi:10.1084/jem.20171419, PMID:29021150.
- [71] Wang G, Ge L, Liu T, Zheng Z, Chen L. The therapeutic potential of arctigenin against multiple human diseases: A mechanistic review. Phytomedicine 2023;110:154647. doi:10.1016/j.phymed.2023.154647, PMID:366
- [72] Zhou S, You H, Qiu S, Yu D, Bai Y, He J, et al. A new perspective on NAFLD: Focusing on the crosstalk between peroxisome proliferator-activated recep-
- Focusing on the crosstalk between peroxisome proliferator-activated receptor alpha (PPARq) and farnesoid X receptor (FXR). Biomed Pharmacother 2022;154:113577. doi:10.1016/j.biopha.2022.113577, PMID:35988420. [73] Ishibashi S, Arai H, Yokote K, Araki E, Suganami H, Yamashita S, et al. Efficacy and safety of pemafibrate (K-877), a selective peroxisome proliferator-activated receptor a modulator, in patients with dyslipidemia: Results from a 24-week, randomized, double blind, active-controlled, phase 3 trial. J Clin Lipidol 2018;12(1):173–184. doi:10.1016/j.jacl.2017.10.006, PMID:32020203 PMID: 29203092